Cell Reports

Report

In utero exposure to NMDA receptor autoantibodies disrupts hippocampal circuit maturation

Graphical abstract

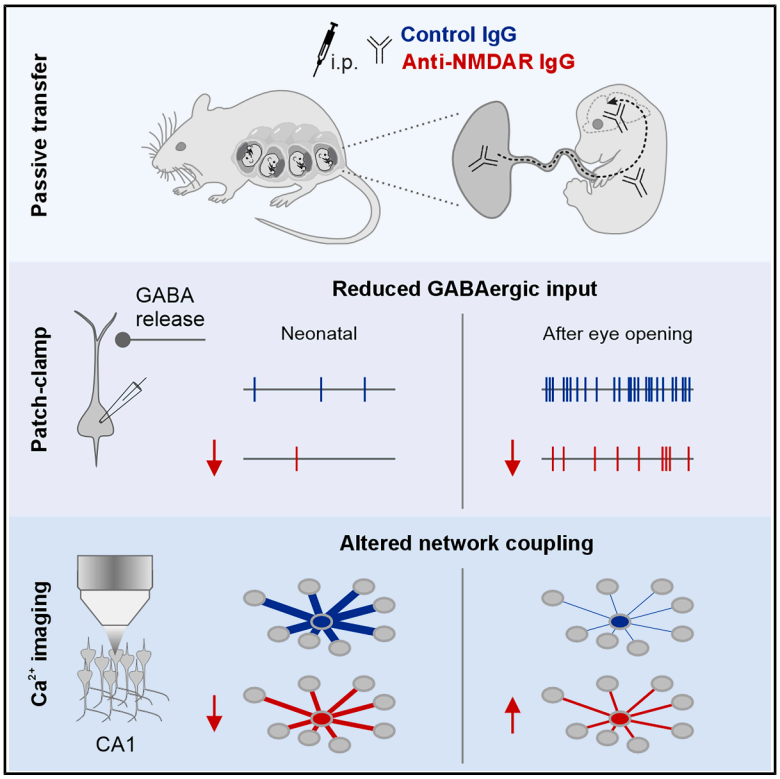

Authors

Myrtill Majoros, Chuanqiang Zhang, Vahid Rahmati, ..., Harald Prüss, Knut Holthoff, Knut Kirmse

Correspondence

knut.kirmse@uni-wuerzburg.de

In brief

Majoros, Zhang, and Rahmati et al. identify a link between maternal autoimmunity and disrupted neuronal network development in the hippocampus of mice. *In utero* exposure to NMDA receptor autoantibodies impairs GABAergic signaling and early network synchrony in neonates, hindering the emergence of continuous hippocampal activity around eye opening.

Highlights

- Maternal NMDA receptor autoantibodies reach the fetal hippocampus in mice
- NMDA receptor autoantibodies disrupt GABAergic synapse development in CA1
- CA1 network synchrony is attenuated in neonates
- NMDA receptor autoantibodies impair the emergence of continuous network dynamics

Majoros et al., 2026, Cell Reports *45*, 117022
March 24, 2026
https://doi.org/10.1016/j.celrep.2026.117022

CellPress

Cell Reports

CellPress
OPEN ACCESS

Report

In utero exposure to NMDA receptor autoantibodies disrupts hippocampal circuit maturation

Myrtill Majoros,[1,2,3,11] Chuanqiang Zhang,[1,11] Vahid Rahmati,[2,11] Jürgen Graf,[2] Manfred Heckmann,[1] Christian Geis,[2] Jakob Kreye,[4,5,6,7,8] Angela M. Kaindl,[6,7,8,9] Harald Prüss,[4,5] Knut Holthoff,[2,10] and Knut Kirmse[1,10,12,*]

[1]Department of Neurophysiology, Institute of Physiology, University of Würzburg, 97070 Würzburg, Germany
[2]Department of Neurology, Jena University Hospital, 07747 Jena, Germany
[3]Institute of Physiology I, Jena University Hospital, 07743 Jena, Germany
[4]German Center for Neurodegenerative Diseases (DZNE), 10117 Berlin, Germany
[5]Department of Neurology and Experimental Neurology, Charité – Universitätsmedizin Berlin, Corporate Member of Freie Universität Berlin and Humboldt-Universität zu Berlin, 10117 Berlin, Germany
[6]Department of Pediatric Neurology, Charité – Universitätsmedizin Berlin, Corporate Member of Freie Universität Berlin and Humboldt-Universität zu Berlin, 13353 Berlin, Germany
[7]Center for Chronically Sick Children, Charité – Universitätsmedizin Berlin, Corporate Member of Freie Universität Berlin and Humboldt-Universität zu Berlin, 13353 Berlin, Germany
[8]German Center for Child and Adolescent Health (DZKJ), Section CNS Development and Neurologic Diseases, Partner Site Berlin, Berlin, Germany
[9]Institute of Cell and Neurobiology, Charité – Universitätsmedizin Berlin, Corporate Member of Freie Universität Berlin and Humboldt-Universität zu Berlin, 10117 Berlin, Germany
[10]Senior author
[11]These authors contributed equally
[12]Lead contact
*Correspondence: knut.kirmse@uni-wuerzburg.de
https://doi.org/10.1016/j.celrep.2026.117022

SUMMARY

Maternal anti-neuronal autoantibodies (ABs) have been linked to abnormal brain maturation and may increase the risk of neurodevelopmental disorders, yet their pathogenetic mechanisms remain elusive. Here, we show that *in utero* exposure to ABs targeting the NR1 subunit of N-methyl-D-aspartate (NMDA) receptors (NR1 ABs) disrupts hippocampal circuit maturation in mice. Using a passive-transfer model, we find that transplacental NR1 ABs impair GABAergic transmission in CA1 pyramidal cells (PCs) *ex vivo*. Ca^{2+} imaging and computational modeling reveal that this deficit compromises early synchronized network activity in neonatal CA1. *In vivo*, NR1 ABs hinder the emergence of continuous activity around eye opening—a critical milestone for later cognitive function—by reducing the ability of CA1 PCs to developmentally decouple from local network dynamics. Our findings implicate NR1 ABs as drivers of a developing hippocampal circuitopathy and highlight disrupted activity-dependent circuit refinement as a mechanistic link between maternal autoimmunity and neurodevelopmental dysfunction.

INTRODUCTION

Anti-neuronal autoantibodies (ABs) have been identified as key pathogenic factors in a growing number of neuropsychiatric disorders.[1,2] Among the most frequently detected are immunoglobulin G (IgG) ABs against N-methyl-D-aspartate receptors (NMDARs), specifically targeting their obligatory NR1 (GluN1) subunit (NR1 ABs).[3] These ABs disrupt NMDAR function and synaptic localization through direct antagonism and cross-linking-induced internalization.[4,5] NMDARs are central components of glutamatergic postsynapses[6] and are also involved in the regulation of GABAergic transmission.[7] By impairing synaptic excitation and inhibition,[8–10] NR1 ABs cause a severe hippocampal circuitopathy—manifested as neuronal hypersynchrony in rodent models[8,10] and underlying epileptic seizures and cognitive dysfunctions in NMDAR encephalitis.[11]

Beyond their pathogenic role in adults, NR1 ABs may also interfere with neuronal development. Starting around gestational week 13 in humans, maternal IgGs are transported across the placenta and accumulate in the fetal circulation.[12] Transplacental ABs access the fetal brain through the immature blood-brain barrier[13] (BBB), creating a critical window for disrupting brain development. Case reports of pregnancies affected by NMDAR encephalitis indicate a potential pathogenic impact of *in utero* NR1 AB exposure.[14,15] Moreover, serum NR1 ABs are occasionally detected in asymptomatic individuals,[16–18] raising concerns about subclinical exposures affecting neurodevelopment in a broader population. While clinical evidence remains limited regarding overall neurodevelopmental outcomes,[19] mechanistic studies underscore the critical roles of NMDARs in synaptic development. Specifically, NMDAR activation was reported to drive the developmental recruitment of AMPA

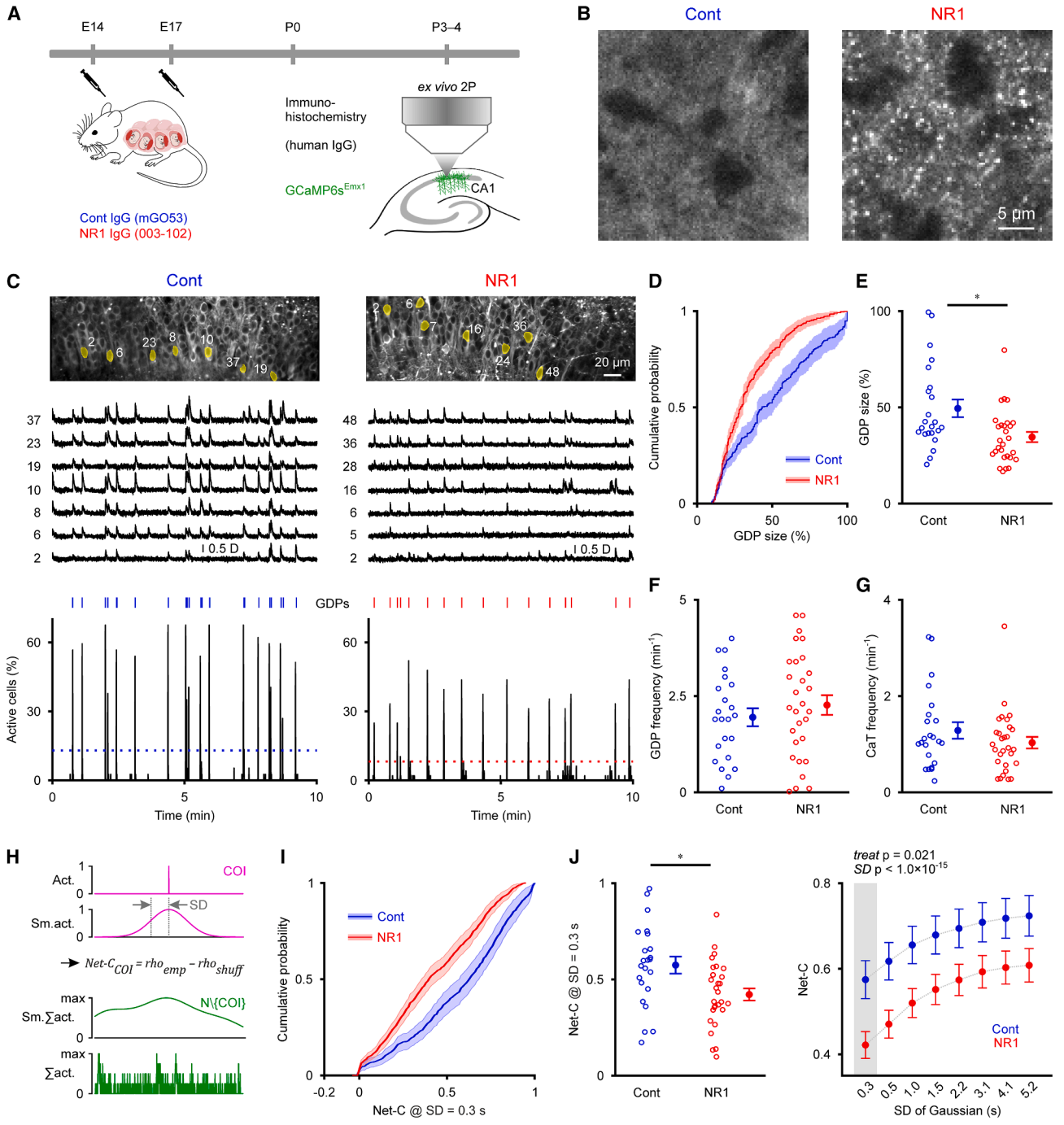

Figure 1. Transplacental NR1 autoantibodies disrupt early synchronized activity in neonatal CA1

(A) Experimental timeline.

(B) Confocal images of human IgG in mouse CA1 stratum lacunosum-moleculare at P0. Note the puncta-like NR1 AB deposits versus diffusely distributed control IgG.

(C) Top: two-photon images of GCaMP6s-expressing CA1 PCs in slices at P3–P4. Middle: sample traces (detection criterion $D(t)$). Bottom: time-aligned percentage of active cells. Dotted lines represent activity-dependent GDP detection thresholds (see STAR Methods). Blue/red markers indicate GDPs.

(D) Cumulative distribution of GDP size (defined as the percentage of cells activated per GDP).

(E) Mean GDP sizes.

(F) GDP frequencies.

(G) Mean CaT frequencies.

(legend continued on next page)

receptors (AMPARs) during glutamatergic synapse unsilencing,[20,21] partly through interactions with depolarizing GABAergic inputs.[22–24] Beyond that, NMDARs are expressed at immature GABAergic contacts,[25] where they are crucial for inhibitory synaptogenesis.[26–29] Disrupting NMDAR function may therefore profoundly affect nascent circuits.[30] Indeed, genetic rodent models with impaired NMDAR signaling exhibit schizophrenia-like phenotypes,[31] and human mutations in *GRIN1* (encoding NR1) cause severe neurodevelopmental disorders.[32,33] Even transient NMDAR blockade in early life induces protracted deficits.[34,35] Recent proof-of-principle studies in mice provide direct evidence that transplacental NR1 ABs impair brain growth and induce reversible or sustained behavioral alterations.[36,37]

Developmental circuit refinements are essential for mature brain function and rely on characteristic early patterns of spontaneous activity that guide synaptic wiring.[38–40] In the rodent hippocampus, this involves an initial perinatal phase of discontinuous activity, in which intermittent synchronized network bursts alternate with long silent periods.[41–45] Around eye opening, hippocampal activity transitions to a continuous regime supporting efficient information processing and behavioral adaptability.[46,47] This activity-dependent maturational milestone relies on coordinated GABAergic and glutamatergic strengthening,[48] which may be susceptible to disruption by maternal NR1 ABs.

Here, we combine a passive-transfer mouse model with *in vivo* acousto-optic Ca^{2+} imaging, *ex vivo* electrophysiology, and computational modeling to demonstrate that maternal NR1 ABs impair GABAergic synaptic development and disrupt key milestones in hippocampal network maturation. Our results identify NR1 ABs as potential drivers of a developing hippocampal circuitopathy, offering mechanistic insights into how maternal autoimmunity may contribute to neuronal and network dysfunction.

RESULTS

Transplacental NR1 ABs disrupt early synchronized activity in neonatal CA1

Pregnant mice received intraperitoneal injections of either human monoclonal IgG1 NR1 ABs (#003-102) or an isotype-matched non-reactive control clone (#mGO53) on embryonic day (E)14 and E17 (240 μg each; Figure 1A). While #mGO53 is an extensively validated negative-control AB, #003-102 targets the NR1 amino-terminal domain, causes direct antagonism and receptor internalization, and is widely employed in autoimmune encephalitis research[5,8,49–54] (see STAR Methods). *In utero* exposure to NR1 ABs was previously shown to decrease NMDAR clusters in neonatal offspring.[36,37] We detected human IgG in all analyzed pups of both treatment groups, confirming successful placental transfer, with ELISA quantification showing average serum concentrations of 30–60 μg/mL and no significant decline from postnatal day (P)0 to P5 (Figure S1A; for statistics, see Table S1). Gestation time, litter size, and postnatal body weight gain were unaffected (Figures S1B–S1D), suggesting that gross physical development is intact. To examine whether transplacental ABs reached the hippocampal CA1 region, we used confocal immunohistochemistry at P0. NR1 ABs were deposited in a puncta-like manner, whereas control IgG was diffusively distributed (Figures 1B and S1E), indicative of receptor-specific binding of NR1 ABs versus non-specific extracellular retention of circulating control IgG in immersion-fixed tissue. In CA1, the highest puncta density was observed in stratum lacunosum-moleculare (Figures S1E and S1F), consistent with synaptogenesis commencing in the distal dendrites of pyramidal cells (PCs).[55,56] Such deposits were further observed in dendritic layers of CA3, the cortical marginal zone, and the thalamus, while their density was low in ontogenetically younger regions, including the cortical plate and dentate gyrus (Figure S1E, left). At P5, NR1 IgG puncta had largely disappeared in CA1, suggesting rapid postnatal clearance, whereas deposits were still observed in CA3, the marginal zone, and the thalamus. Together, considering that BBB permeability to IgG declines sharply after E17,[57] our findings suggest that NR1 IgG binds prenatally in early-maturing regions where synaptic NMDARs are already expressed.

To assess whether transplacental NR1 ABs affect early synchronized activity, we performed *ex vivo* two-photon Ca^{2+} imaging in GCaMP6s-expressing CA1 PCs in slices at P3–P4 (Figure 1C, top). In either treatment group, spontaneous activity consisted of intermittent network bursts (giant depolarizing potentials [GDPs]), alternating with silent periods (Figure 1C, middle).[58] We detected GDPs based on a threshold derived from shuffled data (Figure 1C, bottom) and found that the fraction of active cells per GDP (GDP size) was markedly reduced in NR1 AB-treated neonates as compared to control AB-exposed pups (control: 49.5% ± 4.6%, n = 23 slices with 995 cells, NR1: 34.6% ± 2.7%, n = 28 slices with 1,117 cells, p = 0.010, exact U test; Figures 1D and 1E). This difference was not due to changes in overall activity levels, since both GDP frequencies and mean Ca^{2+} transient (CaT) frequencies (Figures 1F and 1G) were unaltered.

To investigate the mechanism underlying reduced GDP sizes, we first examined the temporal patterning of CaTs. The coefficient variation (CV) of inter-CaT intervals (ICIs) and CV2, a

(H) Network coupling (Net-C) was computed as the Pearson correlation (*rho*) between the smoothed CaT train (Sm.act.) of the cell of interest (COI, top) and the smoothed summed activity (Sm.Σact., middle) of all other analyzed neurons (N\{COI}, bottom). Bias-corrected values were obtained by subtracting *rho* based on surrogate data from *rho* based on empirical data. SD, standard deviation of the Gaussian smoothing kernel.
(I) Cumulative Net-C distribution (SD = 0.3 s).
(J) Left: mean Net-C (SD = 0.3 s). Right: mean Net-C at different SD values. Bias correction involved circular shuffling.
(D and I) Mean (solid lines) ± SEM (shaded areas).
(E–G and J) Open symbols represent individual slices. Population data (closed symbols) are presented as the mean ± SEM. p values refer to significant fixed effects in GLMs. *$p < 0.05$ (fixed effect).
See also Figures S1 and S2 and Table S1.

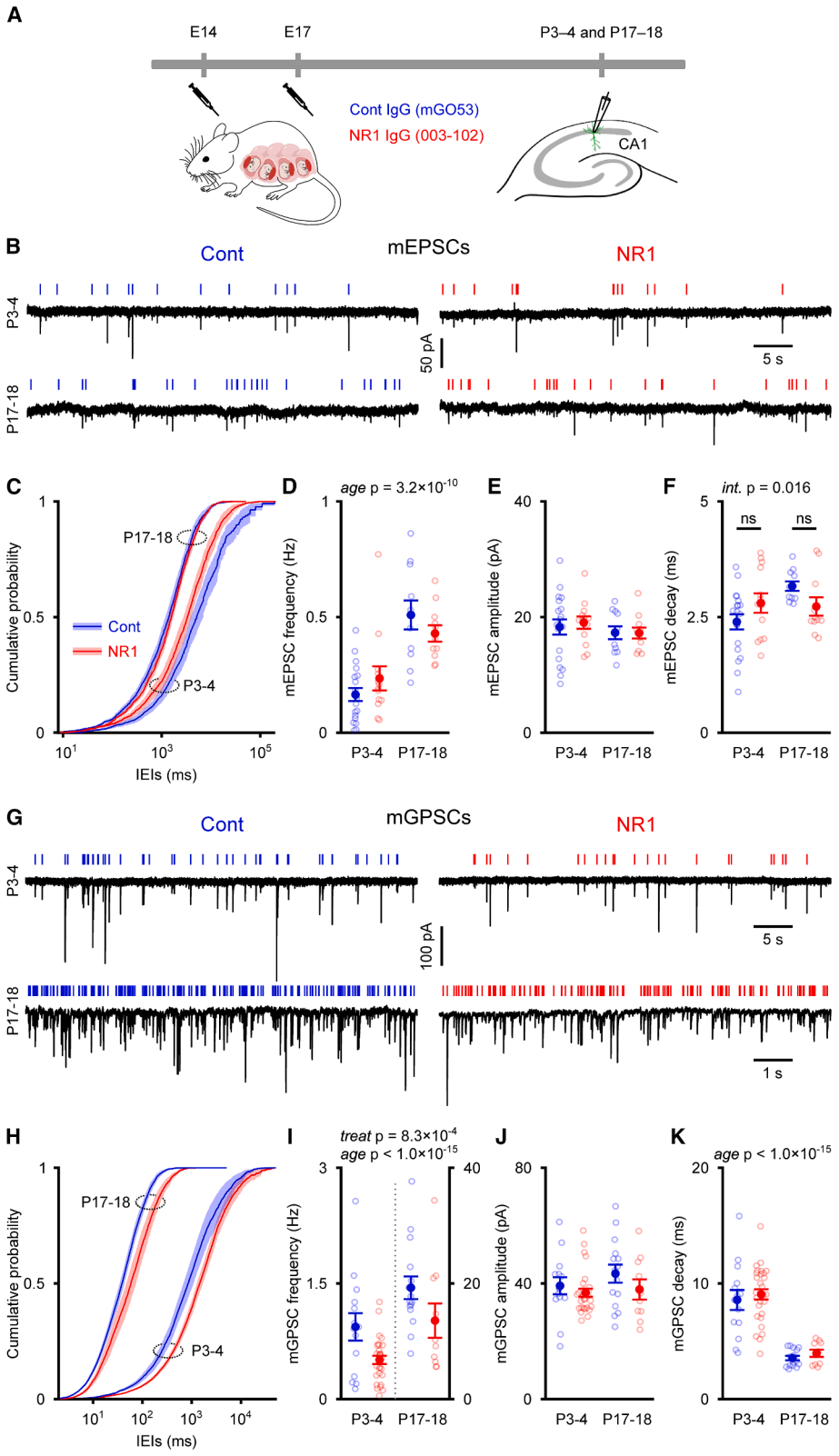

(legend on next page)

local metric of ICI-to-ICI irregularity,[59] were both unchanged (Figures S2B–S2E). We then quantified functional interactions between individual CA1 PCs and the local network using network coupling (Net-C), defined as the Pearson correlation between each neuron's smoothed CaT train and the smoothed sum activity of all other recorded cells (Figure 1H). To control for differences in f_{CaT}, Net-C values were corrected using surrogate data generated by circular shuffling, preserving each neuron's ICIs while disrupting its timing relative to the rest of the population. NR1 ABs caused a marked leftward shift in Net-C distribution and decreased mean Net-C values across a wide range of timescales (standard deviation [SD] of the Gaussian smoothing kernel, 0.3–5.2 s; Figures 1I and 1J). Impaired coupling to the local network was paralleled by a robust decrease in pairwise (neuron-to-neuron) correlation, quantified using the spike time tiling coefficient (STTC; Figures S2F–S2I).[60] In summary, transplacental NR1 ABs disrupt early spontaneous synchronized activity in the hippocampus of newborn mice by reducing Net-C and diminishing coordinated firing among CA1 PCs. This finding stands in sharp contrast to the hypersynchronizing effect of NR1 ABs in adult NMDAR encephalitis.[8,10,11]

Transplacental NR1 ABs induce long-lasting impairments in GABAergic signaling

To elucidate the cellular mechanism underlying the NR1 AB-induced disruption of early synchronized activity, we examined whether impaired NMDAR signaling could account for the network phenotype. In slices from naive mice (P3–P4), acute NMDAR blockade markedly reduced GDP size and frequency (Figures S2J–S2N; Table S2), indicating that spontaneous activity is NMDAR dependent.[61] However, somatic NMDA-induced CaTs did not differ between treatment groups 1 week after the first AB injection (P0), and similar results were obtained at P4–P5 (Figures S2O–S2Q). As NMDARs have been implicated in glutamatergic synapse unsilencing,[20,21,62] we used whole-cell recordings to analyze AMPAR-mediated miniature excitatory postsynaptic currents (mEPSCs) in CA1 PCs at P3–P4 and P17–P18—a period encompassing the developmental surge in synaptogenesis[63] (Figures 2A and 2B). The age-dependent increase in mEPSC frequency, reflecting synaptic connectivity, was unaffected by NR1 ABs (Figures 2C and 2D). Likewise, mEPSC amplitudes, a measure of quantal size, remained unchanged (Figure 2E). Control AB-treated PCs exhibited a developmental slowing of mEPSC decay kinetics that was slightly attenuated by NR1 ABs (interaction: $p = 0.016$, generalized linear model [GLM]), but post hoc contrasts revealed no significant difference in mEPSC half-decay time at either age (Figure 2F). These findings do not support overt glutamatergic deficits but instead point to an alternative mechanism underlying the NR1 AB-induced reduction in GDP size.

As NMDARs also play a key role in GABAergic synaptogenesis,[26–28] we analyzed $GABA_A$ receptor ($GABA_AR$)-mediated miniature postsynaptic currents (mGPSCs) (Figure 2G). At P3–P4, transplacental NR1 ABs decreased mGPSC frequency by ∼50% compared to controls (control: 0.94 ± 0.18, NR1: 0.51 ± 0.05; Figures 2H and 2I). mGPSC frequencies substantially increased in both treatment groups over the next 2 weeks but remained markedly lower in NR1 AB-treated offspring at P17–P18 (control: 19.3 ± 2.0, NR1: 13.6 ± 3.0, treatment: $p = 8.3 \times 10^{-4}$, age: $p < 1.0 \times 10^{-15}$, GLM; Figures 2H and 2I). Conversely, mGPSC amplitudes (Figure 2J) and the developmental acceleration of mGPSC kinetics (Figure 2K) were unchanged. Moreover, NR1 ABs increased the membrane time constant of CA1 PCs ($\tau_{m,PC}$) by ∼50% and ∼20% at P3–P4 and P17–P18, respectively (P3–P4 control: 42.8 ± 3.3 ms, P3–P4 NR1: 64.5 ± 4.4 ms; P17–P18 control: 15.2 ± 1.2 ms, P17–P18 NR1: 18.3 ± 1.3 ms; treatment: $p = 2.1 \times 10^{-5}$, age: $p < 1.0 \times 10^{-15}$, GLM; #16 in Table S2). This increase was mediated by elevated membrane capacitance, while membrane resistance remained unaffected (#17 and #18 in Table S2). In summary, transplacental NR1 ABs induce a lasting deficit in GABAergic synaptic transmission and additionally alter passive membrane properties in CA1 PCs.

Computational network modeling links impaired GABAergic signaling to network pathology

To investigate mechanistic links between circuit-level (Figure 1) and cellular (Figure 2) effects of NR1 ABs, we employed a biophysical CA1 network model of mean firing activities of glutamatergic (PC) and GABAergic interneuron (GIN) populations (A_{PC} and A_{GIN}), with dynamic synaptic weights (Figure 3A, top).[48] The model is experimentally constrained to represent key cellular and network characteristics during the first postnatal week.[58] Upon brief synaptic input, it generates a transient surge

Figure 2. Transplacental NR1 autoantibodies induce long-lasting impairments in GABAergic signaling

(A) Experimental timeline.
(B) Sample traces of AMPAR-mediated mEPSCs recorded from CA1 PCs at P3–P4 and P17–P18. Markers (top) indicate detected events.
(C) Cumulative distribution of mEPSC inter-event intervals (IEIs).
(D) Mean mEPSC frequencies.
(E) Median mEPSC amplitudes.
(F) Mean mEPSC half-decay times.
(G) Sample traces of $GABA_AR$-mediated mGPSCs recorded from CA1 PCs at P3–P4 and P17–P18. Markers (top) indicate detected events.
(H) Cumulative distribution of mGPSC IEIs.
(I) Mean mGPSC frequencies. Note the two *y* axis scales.
(J) Median mGPSC amplitudes.
(K) Mean mGPSC half-decay times.
(C and H) Mean (solid lines) ± SEM (shaded areas).
(D–F and I–K) Open symbols represent individual cells. Population data (closed symbols) are presented as the mean ± SEM. *p* values refer to significant fixed effects in GLMs. ns, not significant (simple contrasts).
See also Figure S2 and Table S2.

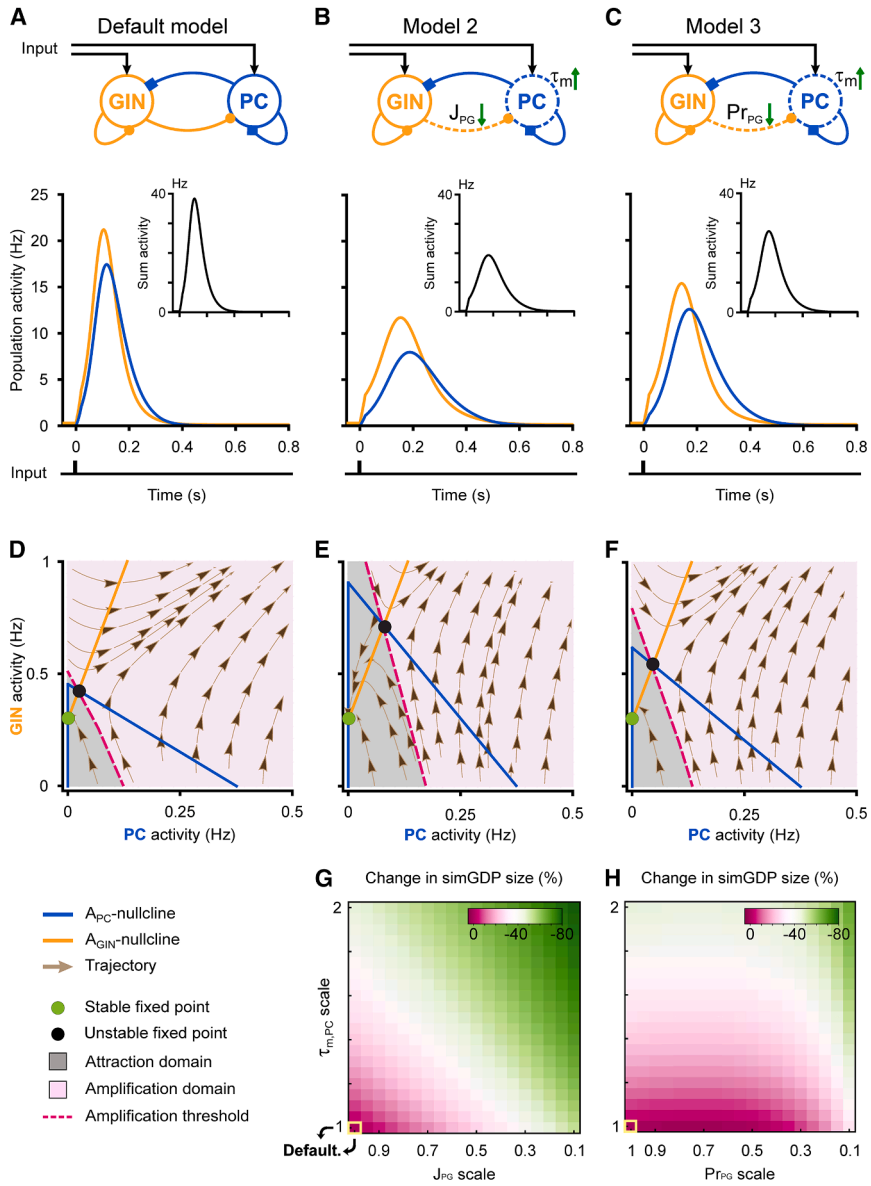

Figure 3. Computational network modeling links impaired GABAergic signaling to network pathology

(A) Top: schematic of the recurrent network model with dynamic synapses (STP-RNN). PC, pyramidal cells; GIN, GABAergic interneurons. Bottom: a simGDP is triggered by a brief depolarizing input (20 ms) to the default network model ($e_{PC} = e_{GIN} = 3$ Hz). Inset: sum of PC (A_{PC}) and GIN (A_{GIN}) population activities. The peak of the summed activity profile defines the simGDP size.

(B and C) An increased membrane time constant of PCs ($\tau_{m,PC}$) and weakened GIN-to-PC synapses (J_{PG}, maximum absolute synaptic efficacy; Pr_{PG}, release probability) reduce simGDP size. The same format as that in (A) is used.

(B) In model 2, $\tau_{m,PC}$ was increased by 50% and J_{PG} was reduced by 50%.

(C) In model 3, $\tau_{m,PC}$ was increased by 50% and Pr_{PG} was decreased by 50%.

(D–F) Steepening of A_{PC}-nullcline in models 2 (E) and 3 (F) contributes to the dampening of network instability dynamics. Each A_{GIN}-A_{PC} plane corresponds to the network shown above (same column) with synaptic efficacies frozen at the rest state (before input arrival; green dot). Brown streamlines show the local direction of example trajectories of these networks.

(G and H) The reduction in simGDP size remains robust across varying levels of increase in $\tau_{m,PC}$ and a decrease in either J_{PG} (G) or Pr_{PG} (H). For each parameter combination, the color represents the corresponding GDP size relative to that in the default model. Parameter scaling was performed by multiplying the corresponding values in the default model by the levels depicted on the axes. Parameter values for all simulations are provided in the STAR Methods.

See also Figure S3.

in network activity resembling GDPs (Figure 3A, bottom). The model enabled us to examine how simulated GDPs (simGDPs) are influenced by factors underlying the NR1 AB-induced reduction in mGPSC frequency and/or increase in $\tau_{m,PC}$. We modeled the decreased mGPSC frequency as a reduction in either the synaptic efficacy (J_{PG}, reflecting release site number) or the release probability (Pr_{PG}) of GIN-to-PC synapses. Reducing J_{PG} by 50% combined with a 50% increase in $\tau_{m,PC}$ markedly diminished simGDP size (model 2 in Figure 3B), mimicking the experimentally observed GDP suppression in NR1 AB-treated pups (Figures 1D and 1E). Likewise, reducing Pr_{PG} by 50%, combined with a 50% increase in $\tau_{m,PC}$, also attenuated simGDP size (model 3 in Figure 3C), albeit the effect was less pronounced than in model 2. Notably, given the relatively low recurrent glutamatergic connectivity in CA1, a sensitivity analysis demonstrated that the differential impact of models 2 and 3 was maintained across a wide range of lower recurrent excitatory synaptic strengths (J_{PP}), confirming the robustness of our results (Figures S3A–S3D). Among the individual parameters, only changes in J_{PG} or $\tau_{m,PC}$, but not Pr_{PG}, were alone sufficient to suppress simGDP size (Figures S3E–S3H).

To investigate what changes in simGDP emergence underlie this behavior, we computed the steady-state A_{GIN}-A_{PC} plane of the network at its rest state (before input arrival; Figure 3D). This analysis assesses the initial phase of network activity following an input perturbation.[48] In addition to a stable fixed point (FP; Figure 3D, green dot) at the rest state, the default model exhibits an unstable FP (Figure 3D, black dot) exposing network activity to an amplification domain (Figure 3D, purple area). Intuitively, simGDPs are effectively triggered only if the input perturbation pushes network activity into this domain. While increased $\tau_{m,PC}$ alone slowed PC population activity (Figure S3H), additionally decreasing J_{PG} steepened the A_{PC}-nullcline in model 2 (Figure 3E), thereby dampening and decelerating

CellPress
OPEN ACCESS

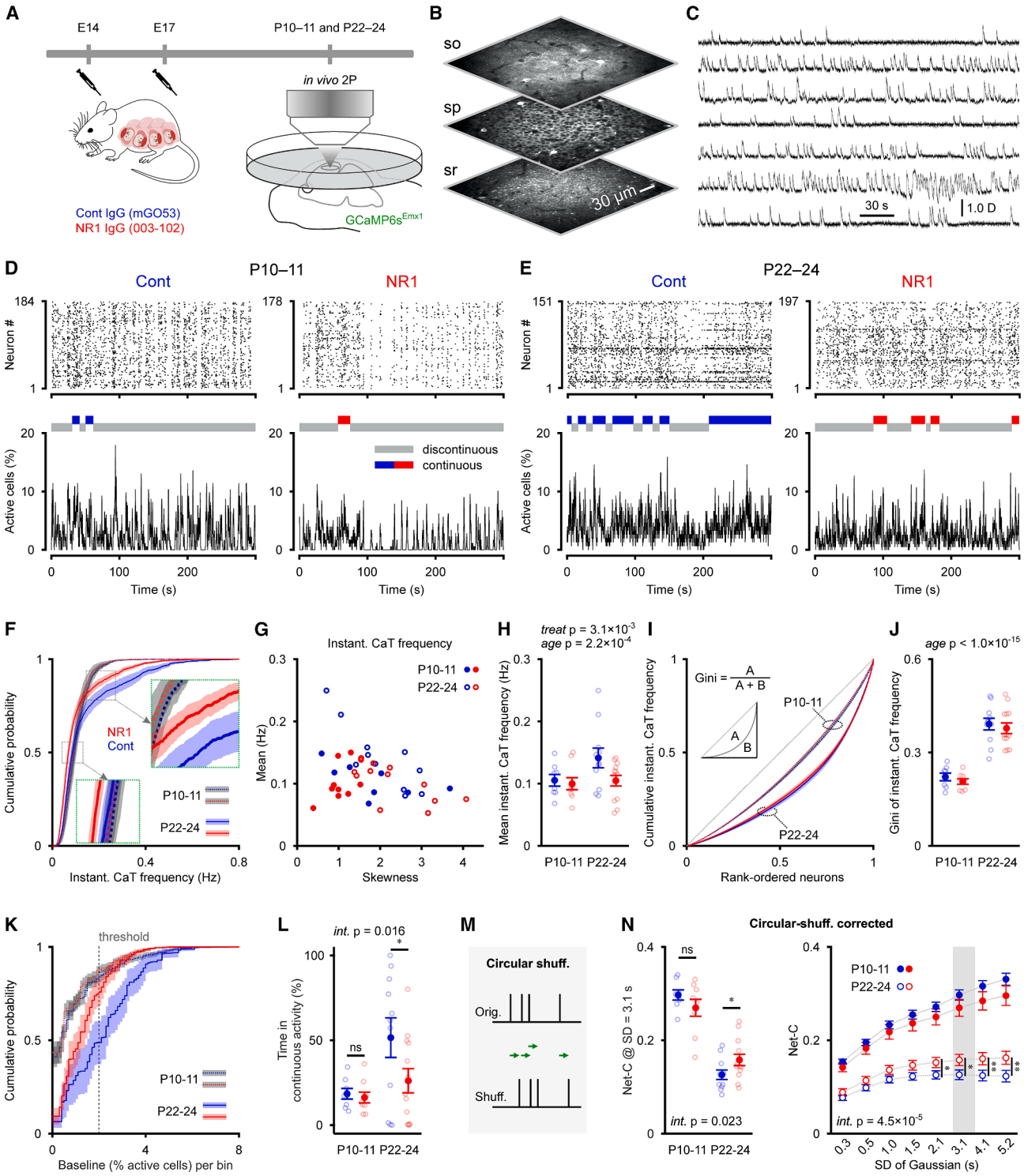

Figure 4. Transplacental NR1 autoantibodies impair hippocampal circuit reorganization during a critical developmental period *in vivo*

(A) Experimental timeline.

(B) Sample *in vivo* two-photon images (so/sp/sr, stratum oriens/pyramidale/radiatum).

(C) Sample traces from several CA1 PCs.

(D and E) Top: raster plots from control or NR1 AB-exposed mice at P10–P11 (D) and P22–P24 (E). Bottom: time-aligned percentage of active cells. Bars indicate time periods classified as either discontinuous or continuous network activity.

(legend continued on next page)

instability dynamics around the unstable FP, ultimately reducing simGDP size (Figure 3B). The steepening of the A_{PC}-nullcline was less pronounced for combined changes in Pr_{PG} and $\tau_{m,PC}$ in model 3 (Figure 3F), explaining its more moderate simGDP suppression (Figure 3C). Importantly, our modeling results remained robust across a broad range of parameter values (Figures 3G and 3H). In sum, computational modeling indicates a key role for reduced GABAergic synaptic efficacy and an increased $\tau_{m,PC}$ in suppressing simGDP size, primarily by harnessing the network's intrinsic instability.

Transplacental NR1 ABs impair hippocampal circuit reorganization during a critical developmental period *in vivo*

Since early synchronized activity guides neuronal circuit development—with the GABAergic strengthening playing a key role[40]—we next asked whether transplacental NR1 ABs disrupt the transition to mature neuronal dynamics. This transition enables PCs to decouple from local network activity around eye opening,[46,47] a prerequisite to support cognitive tasks in adulthood.[38] To address this, we performed *in vivo* acousto-optic Ca^{2+} imaging at P10–P11 (pre-eye opening) and P22–P24 (post-eye opening) (Figures 4A–4C), recording from 6,883 CA1 PCs across 41 mice. Short dwell times minimized photobleaching, allowing extended recordings (58.9 ± 2.8 min).

We first analyzed the firing properties of individual CA1 PCs (Figures 4D–4J). NR1 ABs caused a leftward shift in the distribution of instantaneous CaT frequencies (f_{CaT}), particularly at P22–P24 (Figure 4F). We included f_{CaT} skewness as a covariate in the statistics, given its negative correlation with mean values (Figures 4G and S4A; #27 in Table S3). Mean f_{CaT} increased significantly with age, while NR1 ABs reduced f_{CaT} across development (age: $p = 2.2 \times 10^{-4}$, treatment: $p = 3.1 \times 10^{-3}$; Figure 4H). The developmental increase in f_{CaT} was accompanied by a marked change in distribution shape, transitioning from narrow pre-eye opening to broad and heavy tailed at P22–P24 (Figure 4F). Distributions, where a minority of neurons generate most spikes, are a hallmark of adult networks.[64] Gini coefficients revealed that the developmental redistribution of f_{CaT} was not altered by NR1 ABs (Figures 4I and 4J). To examine the temporal structure of individual CA1 PC firing, we again utilized CV and CV2 of ICIs[59] as measures of global and local spiking irregularity, respectively (Figures S4B–S4E). This analysis revealed an age-dependent transition from a state with more irregular global firing (CV ≈ 1.15) and Poisson-like local behavior (CV2 ≈ 1) to one where global firing stabilizes toward a Poisson-like pattern (CV ≈ 1.0) and local dynamics become more regular (CV2 ≈ 0.9). These trajectories are consistent with CA1 development during this critical period[46] and were similar across treatment groups (Figures S4B–S4E). Collectively, transplacental NR1 ABs disrupt the developmental increase in CaT rates, while their distribution shape and temporal regularity remain unaltered.

A key circuit reconfiguration around eye opening is the emergence of continuous activity, marking the transition from developmental patterns optimized for wiring to mature dynamics supporting efficient information processing.[65–67] This process entails the disappearance of silent periods (Figures 4D and 4E) and relies on the strengthening of recurrent excitation and feedback inhibition.[48,68–70] To examine whether NR1 ABs disrupt this transition, we partitioned recordings into non-overlapping 10-s bins and classified each bin as either continuous or discontinuous based on its baseline activity (Figure 4K; STAR Methods). As this definition depends, by construction, on both CaT timing/distribution and mean CaT rates, we computed the time in continuous activity for both real and CaT-shuffled datasets and used the shuffled values as a covariate for statistical testing. In control AB-treated mice, the time spent in continuous activity was low at P10–P11 but substantially increased toward P22–P24, consistent with findings from naive mice.[46] This maturational milestone was impaired in NR1 AB-exposed littermates, resulting in significantly decreased continuous activity at P22–P24 (interaction: $p = 0.016$; post hoc contrasts: P10–P11: $p = 0.26$, P22–P24: $p = 0.020$, GLM; Figure 4L). We reproduced this finding by an alternative classification approach (#31 in Table S3; STAR Methods). Decreased continuity was not attributable to changes in pairwise coupling, since STTCs declined similarly with age across treatment groups (Figures S4F–S4H). We thus hypothesized that reduced continuity instead reflects altered developmental decoupling of individual CA1 PCs from local network activity. Accordingly, we quantified Net-C of CA1 PCs (cf. Figure 1H), using the circular-shuffling correction. In control AB-treated mice, Net-C decreased sharply around eye opening (Figures 4M and 4N, left). This developmental decoupling was impaired in NR1 AB-exposed littermates, resulting in significantly higher Net-C at P22–P24 (interaction: $p = 0.023$, GLM; post hoc contrasts: P10–P11: $p = 0.37$, P22–P24: $p = 0.014$; Figure 4N, left). To assess the timescale dependence of the effect, we varied SD of the Gaussian smoothing kernel (cf. Figure 1H) and found that the NR1 AB-mediated increase in Net-C was significant for an SD $\geq$ 2.1 s (Figure 4N, right).

(F) Cumulative distributions of instantaneous CaT frequencies (f_{CaT}).
(G) Scatterplot of the mean and the skewness of f_{CaT}. Symbols represent individual mice.
(H) Mean f_{CaT} values were significantly reduced in NR1 AB-treated mice.
(I) Lorenz curves of f_{CaT}. The identity line corresponds to the case in which all CA1 PCs have equal f_{CaT} values.
(J) Gini coefficients.
(K) Cumulative distributions of baseline activity (10-s bins). The vertical line indicates the classification threshold.
(L) At P22–P24, the overall time in continuous activity was significantly reduced in NR1 versus control AB-treated mice.
(M) Graphical representation of circular shuffling.
(N) Left: Net-C profoundly declined from P10–P11 to P22–P24 in control AB-treated mice, but this trajectory was significantly impaired in NR1 AB-treated littermates (SD = 3.1 s). Right: Net-C as a function of SD. Bias correction involved circular shuffling.
(F, I, and K) Mean (solid lines) ± SEM (shaded areas). (H, J, L, and N) Open symbols represent individual mice. Population data (closed symbols) are presented as the mean ± SEM. p values refer to significant fixed effects in GLMs. *$p < 0.05$ and ns, not significant (simple contrasts).
See also Figure S4 and Table S3.

Replacing circular with random shuffling, which preserves mean CaT rates but disrupts ICIs, yielded similar results (Figures S4I and S4J). Finally, we applied event-exchange shuffling to disrupt CaT timing within individual cells while preserving both the summed network activity at each time point and the mean CaT rates (see Figure S4K). The shuffling-subtracted Net-C values dropped near zero across groups (Figure S4L), indicating that the NR1 AB-induced increase in Net-C primarily reflects between-cell timing rather than changes in within-cell temporal dynamics. In summary, *in utero* NR1 AB exposure disrupts the emergence of continuous activity in CA1 *in vivo*. This disruption is closely tied to a reduced developmental decoupling of individual CA1 PCs from local network activity, revealing a key mechanism underlying impaired hippocampal circuit maturation.

DISCUSSION

Our findings show that *in utero* exposure to NR1 ABs disrupts hippocampal circuit maturation, mechanistically linked to a sustained deficit in GABAergic synaptic transmission (Figures 2G–2K). Decreased mGPSC frequencies indicate a decrease in the number of release sites and/or the probability of GABA release. This aligns with accumulating evidence indicating that NMDAR signaling is crucial for GABAergic synapse formation *in vivo*. NMDARs are regularly found at developing GABAergic postsynapses,[25] and their activation enhances synaptogenesis via Ca^{2+}-dependent calmodulin binding to NR1.[28] A likely source of glutamate is spillover from nearby synapses—e.g., input from CA3/CA1 PCs, entorhinal projections,[41] or Cajal-Retzius cells[71]—given the high affinity of NMDARs and the strong glutamatergic drive during neonatal network events.[44] Nevertheless, alternative mechanisms, including non-canonical release from astrocytes,[72] cannot be excluded. Moreover, NMDAR activation is facilitated by depolarizing GABA,[23,44,73] which alone can promote gephyrin clustering and synaptic $GABA_AR$ recruitment.[24] The early onset of the GABAergic deficit (by P3–P4) points to an involvement of dendrite-targeting interneurons, as perisomatic and axoaxonic synapse densities are low at this age.[40,56] This is further supported by the preferential deposition of NR1 ABs in stratum lacunosum-moleculare (Figures S1E and S1F), which mainly receives GABAergic input from oriens-lacunosum-moleculare interneurons and neurogliaform cells,[58,74] alongside glutamatergic input from the entorhinal cortex and thalamus.[41] Neurogliaform cells, in particular, exhibit large synaptic NMDA currents essential for their synaptic integration in CA1.[26] Yet, NMDARs are also critical for perisomatic synaptogenesis, as *GRIN1* deletion in prospective parvalbumin interneurons (PVs) disrupts PV-PC connectivity.[29] This broader role of NMDARs suggests that NR1 ABs may impair multiple inhibitory circuits, potentially contributing to circuitopathy in offspring.

In neonatal mice, the hippocampus does not yet support oscillatory network activity required for spatial navigation, learning, and memory but instead generates intermittent activities, which instruct activity-guided circuit wiring.[39] We found that NR1 ABs weaken neuron-to-network coupling (i.e., Net-C) of CA1 PCs in neonates, thereby decreasing their recruitment during GDPs (Figure 1). This network desynchronization in neonates is in contrast to the hypersynchronizing effects of NR1 ABs in adult rodent models and patients with NMDAR encephalitis.[8,10,11] The opposing effect is likely linked to the depolarizing action of GABA in development, which facilitates early synchronized activity in CA1.[23,44,75] A network model incorporating excitatory GABA supports this view and further suggests that NR1 ABs desynchronize CA1 by decreasing GABAergic release sites and increasing $\tau_{m,PC}$ (Figures 3 and S3). The increased $\tau_{m,PC}$ likely reflects a larger membrane area under space-clamp control, potentially arising from changes in somato-dendritic morphology (e.g., increased soma size, dendritic arborization, and/or spine density). While CA1 glutamatergic synapses appeared unaffected, we cannot rule out alterations in other regions implicated in GDP initiation,[44] including CA3 or cortical areas, which also showed NR1 IgG deposits (Figure S1E). Alterations in these regions might therefore contribute to the observed changes in network dynamics and impaired GABAergic synaptogenesis.

In mice, recognition memory and spatial navigation emerge during the third postnatal week,[76,77] coinciding with the transition from early discontinuous activity to continuous network dynamics.[46,47,78,79] Here, we show that *in utero* exposure to NR1 ABs disrupts this developmental milestone (Figures 4D, 4E, 4K, and 4L). Our findings therefore support a model in which NR1 ABs disrupt activity-guided circuit wiring by suppressing physiologically high neuron-to-network coupling in neonates (Figure 1), thereby driving the network onto a pathological trajectory of excessive coupling and discontinuous network activity post-eye opening (Figure 4). In adulthood, CA1 functions as an inhibition-stabilized network (ISN), in which continuous activity is sustained by relatively strong recurrent excitation balanced by feedback inhibition to maintain stable network dynamics over time.[80] The ISN regime is thought to emerge developmentally[40,48] through a surge in glutamatergic and GABAergic synaptogenesis around eye opening.[45,56,63,81] Given that NR1 ABs markedly reduce mGPSCs (Figures 2G–2K), our findings suggest that erosion of synaptic inhibition causally underlies attenuated continuous activity. This was associated with an impaired developmental increase in firing rates (Figures 4F–4H), possibly reflecting reduced feedback inhibition that pathologically restricts PC activity in favor of preserving network stabilization *in vivo*. These results highlight a critical effect of GABAergic dysfunction on network maturation, grounding hippocampal processing in later life. Notably, the emergence of broad and heavy-tailed firing rate distributions (Figures 4I and 4J) and developmental changes in firing regularity (Figures S4B–S4E) remained unaltered, suggesting that compensatory mechanisms may partially preserve PC firing.

Collectively, our findings identify disrupted activity-dependent circuit reorganization as a key pathomechanism through which transplacental NR1 ABs impair neuronal function and networks during development. We propose that this may reflect a broader principle by which maternal ABs targeting other neuronal proteins contribute to neurodevelopmental deficits. Notably, transplacental ABs against Contactin-associated protein-like 2 (Caspr2),[82,83] synapsin,[84,85] and aquaporin-4[86,87] have been associated with increased risk for autism spectrum disorders and other forms of neurodevelopmental delay. Our findings underscore the need to investigate the convergent and divergent mechanisms by which maternal ABs interfere with

activity-guided brain development and shape vulnerability to neurodevelopmental disease.

Limitations of the study

While NR1 ABs impaired GABAergic postsynaptic currents, potential alterations in interneuron firing and/or chloride homeostasis remain unresolved. Addressing these parameters would be highly informative for a more complete mechanistic understanding of how transplacental NR1 ABs perturb early circuit function. Considering that the adult BBB restricts the entry of circulating ABs into the brain, the developmental effects reported here are unlikely to arise from indirect actions via the mothers' brains. Nevertheless, small NR1 AB amounts may still reach the maternal brain, particularly under conditions of compromised BBB function,[88] and could potentially contribute to offspring phenotypes. Case reports of pregnant patients with NMDAR encephalitis support a pathogenic role of transplacental NR1 ABs,[14,15,89,90] but the spectrum of neurodevelopmental consequences in humans remains elusive. Mothers of children with psychiatric disorders may have higher serum NR1 IgG levels than mothers of unaffected children,[36] yet the diversity of their AB repertoire is unknown. While all pathogenetic NR1 ABs target the NR1 amino-terminal domain, distinct clones differ in their capacity to crosslink receptors and/or antagonize channel function.[5] Direct comparison between the amounts of monoclonal ABs administered in this study with polyclonal responses in humans remains challenging, as this would require reliable measurements of AB-specific concentrations in patient samples, which remain unavailable. Furthermore, while mice provide a valuable model for studying development, cross-species differences in developmental timing need to be considered. Full-term birth in humans corresponds to the time of eye opening in mice (∼P12–P14),[91] a period that aligns with the transition from discontinuous to continuous network dynamics *in vivo*.[70,92–94] In humans, the fetal brain may therefore be exposed to transplacental NR1 ABs for a considerably longer period than in mice. Addressing these species differences in future work will be crucial for translating our findings to human neurodevelopment.

RESOURCE AVAILABILITY

Lead contact

Further information and requests for resources and reagents should be directed to and will be fulfilled by the lead contact, Knut Kirmse (knut.kirmse@uni-wuerzburg.de).

Materials availability

This study did not generate new unique reagents.

Data and code availability

- Data reported in this paper will be shared by the lead contact upon request.
- This paper does not report original code.
- Any additional information required to reanalyze the data reported in this paper is available from the lead contact upon request.

ACKNOWLEDGMENTS

This work was funded by the Deutsche Forschungsgemeinschaft (Research Unit 3004: #432559020 and #415914819 to K.K., H.P., A.M.K., J.K., C.G., and M.H.; Major Research Instrumentation: #502670664 to K.K.; and Research Grants: #442107075 and #448069679 to K.K.), the Schilling Foundation (to C.G.), and the Thüringer Aufbaubank (2017 FGI 0020 to K.H.). We thank Ina Ingrisch (Jena), Maria Oppmann (Würzburg), and Stefanie Bandura (Berlin) for excellent technical assistance.

AUTHOR CONTRIBUTIONS

Conceptualization, K.K., H.P., A.M.K., and J.K.; methodology, M.M., C.Z., J.G., and K.K.; software, V.R., C.Z., and K.K.; formal analysis, M.M., C.Z., V.R., J.K., and K.K.; investigation, M.M. and C.Z.; writing – original draft, K.K., V.R., C.Z., M.M., and M.H.; writing – review & editing, M.M., C.Z., V.R., J.G., M.H., J.K., A.M.K., C.G., H.P., K.H., and K.K.; visualization, V.R., C.Z., M.M., and K.K.; supervision, J.K., A.M.K., C.G., H.P., K.H., and K.K.; project administration, K.K.; funding acquisition, J.K., A.M.K., C.G., H.P., K.H., and K.K.

DECLARATION OF INTERESTS

The authors declare no competing interests.

DECLARATION OF GENERATIVE AI AND AI-ASSISTED TECHNOLOGIES IN THE WRITING PROCESS

During the preparation of this work, the authors used ChatGPT in order to improve language and readability. After using this tool/service, the authors reviewed and edited the content as needed and take full responsibility for the content of the publication.

STAR★METHODS

Detailed methods are provided in the online version of this paper and include the following:

- KEY RESOURCES TABLE
- EXPERIMENTAL MODEL AND STUDY PARTICIPANT DETAILS
- METHOD DETAILS
  - Murine placental passive-transfer model
  - Serum sampling and ELISA quantification
  - Immunohistochemistry and confocal imaging
  - Preparation of acute brain slices
  - Two-photon Ca^{2+} imaging *ex vivo*
  - Patch-clamp recordings *ex vivo*
  - Surgery, anesthesia and animal monitoring
  - Two-photon Ca^{2+} imaging *in vivo*
- QUANTIFICATION AND STATISTICAL ANALYSIS
  - ELISA quantification
  - Immunohistochemistry
  - Patch-clamp recordings
  - Two-photon Ca^{2+} imaging
  - Neural network modeling
  - Statistical analysis

SUPPLEMENTAL INFORMATION

Supplemental information can be found online at https://doi.org/10.1016/j.celrep.2026.117022.

Received: July 23, 2025
Revised: January 16, 2026
Accepted: January 30, 2026
Published: February 19, 2026

REFERENCES

1. Pruss, H. (2021). Autoantibodies in neurological disease. Nat. Rev. Immunol. *21*, 798–813. https://doi.org/10.1038/s41577-021-00543-w.

2. Dalmau, J., Geis, C., and Graus, F. (2017). Autoantibodies to Synaptic Receptors and Neuronal Cell Surface Proteins in Autoimmune Diseases of the Central Nervous System. Physiol. Rev. *97*, 839–887. https://doi.org/10.1152/physrev.00010.2016.

3. Geis, C., Planagumà, J., Carreño, M., Graus, F., and Dalmau, J. (2019). Autoimmune seizures and epilepsy. J. Clin. Investig. *129*, 926–940. https://doi.org/10.1172/JCI125178.

4. Yang, S., Heckmann, J., Taha, A., Gao, S., Steinke, S., Hust, M., Prüß, H., Furukawa, H., Geis, C., Heckmann, M., and Yu-Strzelczyk, J. (2024). It only takes seconds for a human monoclonal autoantibody to inhibit N-methyl-D-aspartate receptors. Preprint at bioRxiv. https://doi.org/10.1101/2024.05.28.595700.

5. Michalski, K., Abdulla, T., Kleeman, S., Schmidl, L., Gómez, R., Simorowski, N., Vallese, F., Prüss, H., Heckmann, M., Geis, C., and Furukawa, H. (2024). Structural and functional mechanisms of anti-NMDAR autoimmune encephalitis. Nat. Struct. Mol. Biol. *31*, 1975–1986. https://doi.org/10.1038/s41594-024-01386-4.

6. Dupuis, J.P., Nicole, O., and Groc, L. (2023). NMDA receptor functions in health and disease: Old actor, new dimensions. Neuron *111*, 2312–2328. https://doi.org/10.1016/j.neuron.2023.05.002.

7. Chiu, C.Q., Martenson, J.S., Yamazaki, M., Natsume, R., Sakimura, K., Tomita, S., Tavalin, S.J., and Higley, M.J. (2018). Input-Specific NMDAR-Dependent Potentiation of Dendritic GABAergic Inhibition. Neuron *97*, 368–377.e3. https://doi.org/10.1016/j.neuron.2017.12.032.

8. Ceanga, M., Rahmati, V., Haselmann, H., Schmidl, L., Hunter, D., Brauer, A.K., Liebscher, S., Kreye, J., Prüss, H., Groc, L., et al. (2023). Human NMDAR autoantibodies disrupt excitatory-inhibitory balance, leading to hippocampal network hypersynchrony. Cell Rep. *42*, 113166. https://doi.org/10.1016/j.celrep.2023.113166.

9. Andrzejak, E., Rabinovitch, E., Kreye, J., Prüss, H., Rosenmund, C., Ziv, N.E., Garner, C.C., and Ackermann, F. (2022). Patient-Derived Anti-NMDAR Antibody Disinhibits Cortical Neuronal Networks through Dysfunction of Inhibitory Neuron Output. J. Neurosci. *42*, 3253–3270. https://doi.org/10.1523/JNEUROSCI.1689-21.2022.

10. Wright, S.K., Rosch, R.E., Wilson, M.A., Upadhya, M.A., Dhangar, D.R., Clarke-Bland, C., Wahid, T.T., Barman, S., Goebels, N., Kreye, J., et al. (2021). Multimodal electrophysiological analyses reveal that reduced synaptic excitatory neurotransmission underlies seizures in a model of NMDAR antibody-mediated encephalitis. Commun. Biol. *4*, 1106. https://doi.org/10.1038/s42003-021-02635-8.

11. Rosch, R.E., Wright, S., Cooray, G., Papadopoulou, M., Goyal, S., Lim, M., Vincent, A., Upton, A.L., Baldeweg, T., and Friston, K.J. (2018). NMDA-receptor antibodies alter cortical microcircuit dynamics. Proc. Natl. Acad. Sci. USA *115*, E9916–E9925. https://doi.org/10.1073/pnas.1804846115.

12. Palmeira, P., Quinello, C., Silveira-Lessa, A.L., Zago, C.A., and Carneiro-Sampaio, M. (2012). IgG placental transfer in healthy and pathological pregnancies. Clin. Dev. Immunol. *2012*, 985646. https://doi.org/10.1155/2012/985646.

13. Braniste, V., Al-Asmakh, M., Kowal, C., Anuar, F., Abbaspour, A., Tóth, M., Korecka, A., Bakocevic, N., Ng, L.G., Kundu, P., et al. (2014). The gut microbiota influences blood-brain barrier permeability in mice. Sci. Transl. Med. *6*, 263ra158. https://doi.org/10.1126/scitranslmed.3009759.

14. Hilderink, M., Titulaer, M.J., Schreurs, M.W.J., Keizer, K., and Bunt, J.E.H. (2015). Transient anti-NMDAR encephalitis in a newborn infant due to transplacental transmission. Neurol. Neuroimmunol. Neuroinflamm. *2*, e126. https://doi.org/10.1212/NXI.0000000000000126.

15. Shi, Y.C., Chen, X.J., Zhang, H.M., Wang, Z., and Du, D.Y. (2017). Anti-N-Methyl-d-Aspartate receptor (NMDAR) encephalitis during pregnancy: Clinical analysis of reported cases. Taiwan. J. Obstet. Gynecol. *56*, 315–319. https://doi.org/10.1016/j.tjog.2017.04.009.

16. Dahm, L., Ott, C., Steiner, J., Stepniak, B., Teegen, B., Saschenbrecker, S., Hammer, C., Borowski, K., Begemann, M., Lemke, S., et al. (2014). Seroprevalence of autoantibodies against brain antigens in health and disease. Ann. Neurol. *76*, 82–94. https://doi.org/10.1002/ana.24189.

17. Lang, K., and Prüss, H. (2017). Frequencies of neuronal autoantibodies in healthy controls: Estimation of disease specificity. Neurol. Neuroimmunol. Neuroinflamm. *4*, e386. https://doi.org/10.1212/NXI.0000000000000386.

18. Hammer, C., Stepniak, B., Schneider, A., Papiol, S., Tantra, M., Begemann, M., Sirén, A.L., Pardo, L.A., Sperling, S., Mohd Jofrry, S., et al. (2014). Neuropsychiatric disease relevance of circulating anti-NMDA receptor autoantibodies depends on blood-brain barrier integrity. Mol. Psychiatr. *19*, 1143–1149. https://doi.org/10.1038/mp.2013.110.

19. Harris, S.L., Binks, S.N.M., Skelly, D., Fourie, H., Cherrington-Walker, P., Bajorek, T., Irani, S.R., Leite, M.I., Handel, A.E., and Al-Diwani, A. (2025). Clinical data and reporting quality in NMDAR-antibody encephalitis and pregnancy: a systematic review. BMJ Neurol. Open *7*, e001005. https://doi.org/10.1136/bmjno-2024-001005.

20. Durand, G.M., Kovalchuk, Y., and Konnerth, A. (1996). Long-term potentiation and functional synapse induction in developing hippocampus. Nature *381*, 71–75. https://doi.org/10.1038/381071a0.

21. Isaac, J.T., Nicoll, R.A., and Malenka, R.C. (1995). Evidence for silent synapses: implications for the expression of LTP. Neuron *15*, 427–434. https://doi.org/10.1016/0896-6273(95)90046-2.

22. Kirmse, K., Kummer, M., Kovalchuk, Y., Witte, O.W., Garaschuk, O., and Holthoff, K. (2015). GABA depolarizes immature neurons and inhibits network activity in the neonatal neocortex in vivo. Nat. Commun. *6*, 7750. https://doi.org/10.1038/ncomms8750.

23. Murata, Y., and Colonnese, M.T. (2020). GABAergic interneurons excite neonatal hippocampus in vivo. Sci. Adv. *6*, eaba1430. https://doi.org/10.1126/sciadv.aba1430.

24. Oh, W.C., Lutzu, S., Castillo, P.E., and Kwon, H.B. (2016). De novo synaptogenesis induced by GABA in the developing mouse cortex. Science *353*, 1037–1040. https://doi.org/10.1126/science.aaf5206.

25. Cserep, C., Szabadits, E., Szonyi, A., Watanabe, M., Freund, T.F., and Nyiri, G. (2012). NMDA receptors in GABAergic synapses during postnatal development. PLoS One *7*, e37753. https://doi.org/10.1371/journal.pone.0037753.

26. Chittajallu, R., Wester, J.C., Craig, M.T., Barksdale, E., Yuan, X.Q., Akgül, G., Fang, C., Collins, D., Hunt, S., Pelkey, K.A., and McBain, C.J. (2017). Afferent specific role of NMDA receptors for the circuit integration of hippocampal neurogliaform cells. Nat. Commun. *8*, 152. https://doi.org/10.1038/s41467-017-00218-y.

27. Deng, R., Chang, M., Kao, J.P.Y., and Kanold, P.O. (2023). Cortical inhibitory but not excitatory synaptic transmission and circuit refinement are altered after the deletion of NMDA receptors during early development. Sci. Rep. *13*, 656. https://doi.org/10.1038/s41598-023-27536-0.

28. Gu, X., Zhou, L., and Lu, W. (2016). An NMDA Receptor-Dependent Mechanism Underlies Inhibitory Synapse Development. Cell Rep. *14*, 471–478. https://doi.org/10.1016/j.celrep.2015.12.061.

29. Singh, M., Sapkota, K., Sakimura, K., Kano, M., Cowell, R.M., Overstreet-Wadiche, L., Hablitz, J.J., and Nakazawa, K. (2023). Maturation of GABAergic Synaptic Transmission From Neocortical Parvalbumin Interneurons Involves N-methyl-D-aspartate Receptor Recruitment of Cav2.1 Channels. Neuroscience *513*, 38–53. https://doi.org/10.1016/j.neuroscience.2023.01.007.

30. Iwasato, T., Datwani, A., Wolf, A.M., Nishiyama, H., Taguchi, Y., Tonegawa, S., Knöpfel, T., Erzurumlu, R.S., and Itohara, S. (2000). Cortex-restricted disruption of NMDAR1 impairs neuronal patterns in the barrel cortex. Nature *406*, 726–731. https://doi.org/10.1038/35021059.

31. Mohn, A.R., Gainetdinov, R.R., Caron, M.G., and Koller, B.H. (1999). Mice with reduced NMDA receptor expression display behaviors related to schizophrenia. Cell *98*, 427–436. https://doi.org/10.1016/s0092-8674(00)81972-8.

32. Epi4K Consortium; Epilepsy Phenome/Genome Project; Allen, A.S., Berkovic, S.F., Cossette, P., Delanty, N., Dlugos, D., Eichler, E.E., Epstein, M.P., Glauser, T., et al. (2013). De novo mutations in epileptic encephalopathies. Nature *501*, 217–221. https://doi.org/10.1038/nature12439.

33. Chen, W., Shieh, C., Swanger, S.A., Tankovic, A., Au, M., McGuire, M., Tagliati, M., Graham, J.M., Madan-Khetarpal, S., Traynelis, S.F., et al. (2017). GRIN1 mutation associated with intellectual disability alters NMDA receptor trafficking and function. J. Hum. Genet. *62*, 589–597. https://doi.org/10.1038/jhg.2017.19.

34. Stefani, M.R., and Moghaddam, B. (2005). Transient N-methyl-D-aspartate receptor blockade in early development causes lasting cognitive deficits relevant to schizophrenia. Biol. Psychiatry *57*, 433–436. https://doi.org/10.1016/j.biopsych.2004.11.031.

35. Kaindl, A.M., Koppelstaetter, A., Nebrich, G., Stuwe, J., Sifringer, M., Zabel, C., Klose, J., and Ikonomidou, C. (2008). Brief alteration of NMDA or GABAA receptor-mediated neurotransmission has long term effects on the developing cerebral cortex. Mol. Cell. Proteomics *7*, 2293–2310. https://doi.org/10.1074/mcp.M800030-MCP200.

36. Jurek, B., Chayka, M., Kreye, J., Lang, K., Kraus, L., Fidzinski, P., Kornau, H.C., Dao, L.M., Wenke, N.K., Long, M., et al. (2019). Human gestational N-methyl-d-aspartate receptor autoantibodies impair neonatal murine brain function. Ann. Neurol. *86*, 656–670. https://doi.org/10.1002/ana.25552.

37. Garcia-Serra, A., Radosevic, M., Pupak, A., Brito, V., Rios, J., Aguilar, E., Maudes, E., Arino, H., Spatola, M., Mannara, F., et al. (2021). Placental transfer of NMDAR antibodies causes reversible alterations in mice. Neurol Neuroimmunol Neuroinflamm *8*. https://doi.org/10.1212/NXI.0000000000000915.

38. Wu, M.W., Kourdougli, N., and Portera-Cailliau, C. (2024). Network state transitions during cortical development. Nat. Rev. Neurosci. *25*, 535–552. https://doi.org/10.1038/s41583-024-00824-y.

39. Cossart, R., and Khazipov, R. (2022). How development sculpts hippocampal circuits and function. Physiol. Rev. *102*, 343–378. https://doi.org/10.1152/physrev.00044.2020.

40. Kirmse, K., and Zhang, C. (2022). Principles of GABAergic signaling in developing cortical network dynamics. Cell Rep. *38*, 110568. https://doi.org/10.1016/j.celrep.2022.110568.

41. Leprince, E., Dard, R.F., Mortet, S., Filippi, C., Giorgi-Kurz, M., Bourboulou, R., Lenck-Santini, P.P., Picardo, M.A., Bocchio, M., Baude, A., and Cossart, R. (2023). Extrinsic control of the early postnatal CA1 hippocampal circuits. Neuron *111*, 888–902.e8. https://doi.org/10.1016/j.neuron.2022.12.013.

42. Mohns, E.J., and Blumberg, M.S. (2008). Synchronous bursts of neuronal activity in the developing hippocampus: modulation by active sleep and association with emerging gamma and theta rhythms. J. Neurosci. *28*, 10134–10144. https://doi.org/10.1523/JNEUROSCI.1967-08.2008.

43. Leinekugel, X., Khazipov, R., Cannon, R., Hirase, H., Ben-Ari, Y., and Buzsáki, G. (2002). Correlated bursts of activity in the neonatal hippocampus in vivo. Science *296*, 2049–2052. https://doi.org/10.1126/science.1071111.

44. Graf, J., Zhang, C., Marguet, S.L., Herrmann, T., Flossmann, T., Hinsch, R., Rahmati, V., Guenther, M., Frahm, C., Urbach, A., et al. (2021). A limited role of NKCC1 in telencephalic glutamatergic neurons for developing hippocampal network dynamics and behavior. Proc. Natl. Acad. Sci. USA *118*, e2014784118. https://doi.org/10.1073/pnas.2014784118.

45. Dard, R.F., Leprince, E., Denis, J., Rao Balappa, S., Suchkov, D., Boyce, R., Lopez, C., Giorgi-Kurz, M., Szwagier, T., Dumont, T., et al. (2022). The rapid developmental rise of somatic inhibition disengages hippocampal dynamics from self-motion. eLife *11*, e78116. https://doi.org/10.7554/eLife.78116.

46. Graf, J., Rahmati, V., Majoros, M., Witte, O.W., Geis, C., Kiebel, S.J., Holthoff, K., and Kirmse, K. (2022). Network instability dynamics drive a transient bursting period in the developing hippocampus in vivo. eLife *11*, e82756. https://doi.org/10.7554/eLife.82756.

47. Pochinok, I., Stöber, T.M., Triesch, J., Chini, M., and Hanganu-Opatz, I.L. (2024). A developmental increase of inhibition promotes the emergence of hippocampal ripples. Nat. Commun. *15*, 738. https://doi.org/10.1038/s41467-024-44983-z.

48. Rahmati, V., Kirmse, K., Holthoff, K., Schwabe, L., and Kiebel, S.J. (2017). Developmental Emergence of Sparse Coding: A Dynamic Systems Approach. Sci. Rep. *7*, 13015. https://doi.org/10.1038/s41598-017-13468-z.

49. Kreye, J., Wenke, N.K., Chayka, M., Leubner, J., Murugan, R., Maier, N., Jurek, B., Ly, L.T., Brandl, D., Rost, B.R., et al. (2016). Human cerebrospinal fluid monoclonal N-methyl-D-aspartate receptor autoantibodies are sufficient for encephalitis pathogenesis. Brain *139*, 2641–2652. https://doi.org/10.1093/brain/aww208.

50. Wardemann, H., Yurasov, S., Schaefer, A., Young, J.W., Meffre, E., and Nussenzweig, M.C. (2003). Predominant autoantibody production by early human B cell precursors. Science *301*, 1374–1377. https://doi.org/10.1126/science.1086907.

51. Jamet, Z., Mergaux, C., Meras, M., Bouchet, D., Villega, F., Kreye, J., Prüss, H., and Groc, L. (2024). NMDA receptor autoantibodies primarily impair the extrasynaptic compartment. Brain *147*, 2745–2760. https://doi.org/10.1093/brain/awae163.

52. Steinke, S., Kirmann, T., Loi, E.A., Nerlich, J., Weichard, I., Kuhn, P., Bullmann, T., Ritzau-Jost, A., Rizalar, F.S., Prüss, H., et al. (2023). NMDA-receptor-Fc-fusion constructs neutralize anti-NMDA receptor antibodies. Brain *146*, 1812–1820. https://doi.org/10.1093/brain/awac497.

53. Reincke, S.M., von Wardenburg, N., Homeyer, M.A., Kornau, H.C., Spagni, G., Li, L.Y., Kreye, J., Sánchez-Sendín, E., Blumenau, S., Stappert, D., et al. (2023). Chimeric autoantibody receptor T cells deplete NMDA receptor-specific B cells. Cell *186*, 5084–5097.e18. https://doi.org/10.1016/j.cell.2023.10.001.

54. Kanno, A., Kito, T., Maeda, M., Yamaki, S., Amano, Y., Shimomura, T., Anisimova, M., Kanazawa, N., Suzuki, K., Razai, A., et al. (2025). Monoclonal humanized monovalent antibody blocking therapy for anti-NMDA receptor encephalitis. Nat. Commun. *16*, 5292. https://doi.org/10.1038/s41467-025-60628-1.

55. Tyzio, R., Represa, A., Jorquera, I., Ben-Ari, Y., Gozlan, H., and Aniksztejn, L. (1999). The establishment of GABAergic and glutamatergic synapses on CA1 pyramidal neurons is sequential and correlates with the development of the apical dendrite. J. Neurosci. *19*, 10372–10382. https://doi.org/10.1523/JNEUROSCI.19-23-10372.1999.

56. Marty, S., Wehrlé, R., Alvarez-Leefmans, F.J., Gasnier, B., and Sotelo, C. (2002). Postnatal maturation of Na+, K+, 2Cl- cotransporter expression and inhibitory synaptogenesis in the rat hippocampus: an immunocytochemical analysis. Eur. J. Neurosci. *15*, 233–245. https://doi.org/10.1046/j.0953-816x.2001.01854.x.

57. Kowal, C., Athanassiou, A., Chen, H., and Diamond, B. (2015). Maternal antibodies and developing blood-brain barrier. Immunol. Res. *63*, 18–25. https://doi.org/10.1007/s12026-015-8714-5.

58. Flossmann, T., Kaas, T., Rahmati, V., Kiebel, S.J., Witte, O.W., Holthoff, K., and Kirmse, K. (2019). Somatostatin Interneurons Promote Neuronal Synchrony in the Neonatal Hippocampus. Cell Rep. *26*, 3173–3182.e5. https://doi.org/10.1016/j.celrep.2019.02.061.

59. Holt, G.R., Softky, W.R., Koch, C., and Douglas, R.J. (1996). Comparison of discharge variability in vitro and in vivo in cat visual cortex neurons. J. Neurophysiol. *75*, 1806–1814. https://doi.org/10.1152/jn.1996.75.5.1806.

60. Cutts, C.S., and Eglen, S.J. (2014). Detecting pairwise correlations in spike trains: an objective comparison of methods and application to the study of retinal waves. J. Neurosci. *34*, 14288–14303. https://doi.org/10.1523/JNEUROSCI.2767-14.2014.

61. Mizuno, H., Rao, M.S., Mizuno, H., Sato, T., Nakazawa, S., and Iwasato, T. (2021). NMDA Receptor Enhances Correlation of Spontaneous Activity in Neonatal Barrel Cortex. J. Neurosci. *41*, 1207–1217. https://doi.org/10.1523/JNEUROSCI.0527-20.2020.

62. Adesnik, H., Li, G., During, M.J., Pleasure, S.J., and Nicoll, R.A. (2008). NMDA receptors inhibit synapse unsilencing during brain development. Proc. Natl. Acad. Sci. USA *105*, 5597–5602. https://doi.org/10.1073/pnas.0800946105.

63. Horton, S., Mastrolia, V., Jackson, R.E., Kemlo, S., Pereira Machado, P.M., Carbajal, M.A., Hindges, R., Fleck, R.A., Aguiar, P., Neves, G., and Burrone, J. (2024). Excitatory and inhibitory synapses show a tight subcellular correlation that weakens over development. Cell Rep. *43*, 114361. https://doi.org/10.1016/j.celrep.2024.114361.

64. Buzsaki, G., and Mizuseki, K. (2014). The log-dynamic brain: how skewed distributions affect network operations. Nat. Rev. Neurosci. *15*, 264–278. https://doi.org/10.1038/nrn3687.

65. Boran, E., Fedele, T., Klaver, P., Hilfiker, P., Stieglitz, L., Grunwald, T., and Sarnthein, J. (2019). Persistent hippocampal neural firing and hippocampal-cortical coupling predict verbal working memory load. Sci. Adv. *5*, eaav3687. https://doi.org/10.1126/sciadv.aav3687.

66. Zylberberg, J., and Strowbridge, B.W. (2017). Mechanisms of Persistent Activity in Cortical Circuits: Possible Neural Substrates for Working Memory. Annu. Rev. Neurosci. *40*, 603–627. https://doi.org/10.1146/annurev-neuro-070815-014006.

67. Barbosa, J., Stein, H., Martinez, R.L., Galan-Gadea, A., Li, S., Dalmau, J., Adam, K.C.S., Valls-Solé, J., Constantinidis, C., and Compte, A. (2020). Interplay between persistent activity and activity-silent dynamics in the prefrontal cortex underlies serial biases in working memory. Nat. Neurosci. *23*, 1016–1024. https://doi.org/10.1038/s41593-020-0644-4.

68. Chini, M., Pfeffer, T., and Hanganu-Opatz, I. (2022). An increase of inhibition drives the developmental decorrelation of neural activity. eLife *11*, e78811. https://doi.org/10.7554/eLife.78811.

69. Colonnese, M.T. (2014). Rapid developmental emergence of stable depolarization during wakefulness by inhibitory balancing of cortical network excitability. J. Neurosci. *34*, 5477–5485. https://doi.org/10.1523/JNEUROSCI.3659-13.2014.

70. Colonnese, M.T., Kaminska, A., Minlebaev, M., Milh, M., Bloem, B., Lescure, S., Moriette, G., Chiron, C., Ben-Ari, Y., and Khazipov, R. (2010). A conserved switch in sensory processing prepares developing neocortex for vision. Neuron *67*, 480–498. https://doi.org/10.1016/j.neuron.2010.07.015.

71. Quattrocolo, G., and Maccaferri, G. (2014). Optogenetic activation of cajal-retzius cells reveals their glutamatergic output and a novel feedforward circuit in the developing mouse hippocampus. J. Neurosci. *34*, 13018–13032. https://doi.org/10.1523/JNEUROSCI.1407-14.2014.

72. de Ceglia, R., Ledonne, A., Litvin, D.G., Lind, B.L., Carriero, G., Latagliata, E.C., Bindocci, E., Di Castro, M.A., Savtchouk, I., Vitali, I., et al. (2023). Specialized astrocytes mediate glutamatergic gliotransmission in the CNS. Nature *622*, 120–129. https://doi.org/10.1038/s41586-023-06502-w.

73. Leinekugel, X., Medina, I., Khalilov, I., Ben-Ari, Y., and Khazipov, R. (1997). Ca2+ oscillations mediated by the synergistic excitatory actions of GABA(A) and NMDA receptors in the neonatal hippocampus. Neuron *18*, 243–255. https://doi.org/10.1016/s0896-6273(00)80265-2.

74. Tricoire, L., Pelkey, K.A., Erkkila, B.E., Jeffries, B.W., Yuan, X., and McBain, C.J. (2011). A blueprint for the spatiotemporal origins of mouse hippocampal interneuron diversity. J. Neurosci. *31*, 10948–10970. https://doi.org/10.1523/JNEUROSCI.0323-11.2011.

75. Spoljaric, I., Spoljaric, A., Mavrovic, M., Seja, P., Puskarjov, M., and Kaila, K. (2019). KCC2-Mediated Cl(-) Extrusion Modulates Spontaneous Hippocampal Network Events in Perinatal Rats and Mice. Cell Rep. *26*, 1073–1081.e3. https://doi.org/10.1016/j.celrep.2019.01.011.

76. Albani, S.H., McHail, D.G., and Dumas, T.C. (2014). Developmental studies of the hippocampus and hippocampal-dependent behaviors: insights from interdisciplinary studies and tips for new investigators. Neurosci. Biobehav. Rev. *43*, 183–190. https://doi.org/10.1016/j.neubiorev.2014.04.009.

77. Brust, V., Schindler, P.M., and Lewejohann, L. (2015). Lifetime development of behavioural phenotype in the house mouse (Mus musculus). Front. Zool. *12*, S17. https://doi.org/10.1186/1742-9994-12-S1-S17.

78. Buhl, D.L., and Buzsáki, G. (2005). Developmental emergence of hippocampal fast-field "ripple" oscillations in the behaving rat pups. Neuroscience *134*, 1423–1430. https://doi.org/10.1016/j.neuroscience.2005.05.030.

79. Stark, E., Roux, L., Eichler, R., Senzai, Y., Royer, S., and Buzsáki, G. (2014). Pyramidal cell-interneuron interactions underlie hippocampal ripple oscillations. Neuron *83*, 467–480. https://doi.org/10.1016/j.neuron.2014.06.023.

80. Watkins de Jong, L., Nejad, M.M., Yoon, E., Cheng, S., and Diba, K. (2023). Optogenetics reveals paradoxical network stabilizations in hippocampal CA1 and CA3. Curr. Biol. *33*, 1689–1703.e5. https://doi.org/10.1016/j.cub.2023.03.032.

81. Fiala, J.C., Feinberg, M., Popov, V., and Harris, K.M. (1998). Synaptogenesis via dendritic filopodia in developing hippocampal area CA1. J. Neurosci. *18*, 8900–8911. https://doi.org/10.1523/JNEUROSCI.18-21-08900.1998.

82. Brimberg, L., Mader, S., Jeganathan, V., Berlin, R., Coleman, T.R., Gregersen, P.K., Huerta, P.T., Volpe, B.T., and Diamond, B. (2016). Caspr2-reactive antibody cloned from a mother of an ASD child mediates an ASD-like phenotype in mice. Mol. Psychiatr. *21*, 1663–1671. https://doi.org/10.1038/mp.2016.165.

83. Su, J., Gupta, R., van Hoof, S., Kreye, J., Pruss, H., Spielman, B., Brimberg, L., Volpe, B.T., Huerta, P.T., and Diamond, B. (2025). Heterogeneity of anti-Caspr2 antibodies: specificity and pathogenicity. Transl Psychiatry *15*, 498. https://doi.org/10.1038/s41398-025-03677-w.

84. Bunger, I., Talucci, I., Kreye, J., Holtje, M., Makridis, K.L., Foverskov Rasmussen, H., van Hoof, S., Cordero-Gomez, C., Ullrich, T., Sedlin, E., et al. (2023). Synapsin autoantibodies during pregnancy are associated with fetal abnormalities. Brain Behav Immun Health *33*, 100678. https://doi.org/10.1016/j.bbih.2023.100678.

85. Bunger, I., Makridis, K.L., Kreye, J., Nikolaus, M., Sedlin, E., Ullrich, T., Hoffmann, C., Tromm, J.V., Rasmussen, H.F., Milovanovic, D., et al. (2023). Maternal synapsin autoantibodies are associated with neurodevelopmental delay. Front. Immunol. *14*, 1101087. https://doi.org/10.3389/fimmu.2023.1101087.

86. Nour, M.M., Nakashima, I., Coutinho, E., Woodhall, M., Sousa, F., Revis, J., Takai, Y., George, J., Kitley, J., Santos, M.E., et al. (2016). Pregnancy outcomes in aquaporin-4-positive neuromyelitis optica spectrum disorder. Neurology *86*, 79–87. https://doi.org/10.1212/WNL.0000000000002208.

87. Mader, S., Brimberg, L., Vo, A., Strohl, J.J., Crawford, J.M., Bonnin, A., Carrión, J., Campbell, D., Huerta, T.S., La Bella, A., et al. (2022). In utero exposure to maternal anti-aquaporin-4 antibodies alters brain vasculature and neural dynamics in male mouse offspring. Sci. Transl. Med. *14*, eabe9726. https://doi.org/10.1126/scitranslmed.abe9726.

88. Castillo-Gomez, E., Kästner, A., Steiner, J., Schneider, A., Hettling, B., Poggi, G., Ostehr, K., Uhr, M., Asif, A.R., Matzke, M., et al. (2016). The brain as immunoprecipitator of serum autoantibodies against N-Methyl-D-aspartate receptor subunit NR1. Ann. Neurol. *79*, 144–151. https://doi.org/10.1002/ana.24545.

89. Ueda, A., Nagao, R., Maeda, T., Kikuchi, K., Murate, K., Niimi, Y., Shima, S., and Mutoh, T. (2017). Absence of serum anti-NMDAR antibodies in anti-NMDAR encephalitis mother predicts having healthy newborn. Clin. Neurol. Neurosurg. *161*, 14–16. https://doi.org/10.1016/j.clineuro.2017.07.012.

90. Chourasia, N., Watkins, M.W., Lankford, J.E., Kass, J.S., and Kamdar, A. (2018). An Infant Born to a Mother With Anti-N-Methyl-d-Aspartate Receptor Encephalitis. Pediatr. Neurol. *79*, 65–68. https://doi.org/10.1016/j.pediatrneurol.2017.11.010.

91. Romijn, H.J., Hofman, M.A., and Gramsbergen, A. (1991). At what age is the developing cerebral cortex of the rat comparable to that of the

full-term newborn human baby? Early Hum. Dev. *26*, 61–67. https://doi.org/10.1016/0378-3782(91)90044-4.

92. Milh, M., Kaminska, A., Huon, C., Lapillonne, A., Ben-Ari, Y., and Khazipov, R. (2007). Rapid cortical oscillations and early motor activity in premature human neonate. Cereb. Cortex *17*, 1582–1594. https://doi.org/10.1093/cercor/bhl069.
93. Vanhatalo, S., Palva, J.M., Andersson, S., Rivera, C., Voipio, J., and Kaila, K. (2005). Slow endogenous activity transients and developmental expression of K+-Cl- cotransporter 2 in the immature human cortex. Eur. J. Neurosci. *22*, 2799–2804. https://doi.org/10.1111/j.1460-9568.2005.04459.x.
94. Arichi, T., Whitehead, K., Barone, G., Pressler, R., Padormo, F., Edwards, A.D., and Fabrizi, L. (2017). Localization of spontaneous bursting neuronal activity in the preterm human brain with simultaneous EEG-fMRI. eLife *6*, e27814. https://doi.org/10.7554/eLife.27814.
95. Pnevmatikakis, E.A., and Giovannucci, A. (2017). NoRMCorre: An online algorithm for piecewise rigid motion correction of calcium imaging data. J. Neurosci. Methods *291*, 83–94. https://doi.org/10.1016/j.jneumeth.2017.07.031.
96. Sweeney, Y., and Clopath, C. (2020). Population coupling predicts the plasticity of stimulus responses in cortical circuits. eLife *9*, e56053. https://doi.org/10.7554/eLife.56053.
97. Okun, M., Steinmetz, N., Cossell, L., Iacaruso, M.F., Ko, H., Barthó, P., Moore, T., Hofer, S.B., Mrsic-Flogel, T.D., Carandini, M., and Harris, K.D. (2015). Diverse coupling of neurons to populations in sensory cortex. Nature *521*, 511–515. https://doi.org/10.1038/nature14273.
98. Tsodyks, M., Pawelzik, K., and Markram, H. (1998). Neural networks with dynamic synapses. Neural Comput. *10*, 821–835. https://doi.org/10.1162/089976698300017502.
99. Garaschuk, O., Hanse, E., and Konnerth, A. (1998). Developmental profile and synaptic origin of early network oscillations in the CA1 region of rat neonatal hippocampus. J. Physiol. *507*, 219–236. https://doi.org/10.1111/j.1469-7793.1998.219bu.x.
100. Menendez de la Prida, L., Bolea, S., and Sanchez-Andres, J.V. (1998). Origin of the synchronized network activity in the rabbit developing hippocampus. Eur. J. Neurosci. *10*, 899–906. https://doi.org/10.1046/j.1460-9568.1998.00097.x.

STAR★METHODS

KEY RESOURCES TABLE

REAGENT or RESOURCE	SOURCE	IDENTIFIER
Antibodies		
Human IgG1 anti-NR1 (clone #003–102)	Kreye et al.[49]	N/A
Human non-reactive IgG1 (clone #mGO53)	Wardemann et al.[50]	N/A
Goat anti-human IgG (H + L) Cross-Absorbed Secondary Antibody, Alexa Fluor 647	Invitrogen	Cat#A-21445; RRID: AB_2535862
mouse anti-human IgG (clone MT145)	Mabtech	RRID: AB_10697677
mouse anti-human IgG-ALP (clone MT78)	Mabtech	RRID: AB_10697678
Chemicals, peptides, and recombinant proteins		
DNQX	Tocris Bioscience	Cat#0189; Cas#2379-57-9
Gabazine (SR 95531 hydrobromide)	Tocris Bioscience	Cat#1262; Cas#104104-50-9
D-APV	Tocris Bioscience	Cat#0106; Cas#79055-68-8
DL-APV	Tocris Bioscience	Cat#0105; Cas#76326-31-3
DL-APV	HelloBio	Cat#HB0251; Cas#76326-31-3
Nifedipine	Sigma-Aldrich	Cat#N7634; Cas#21829-25-4
NMDA	Tocris Bioscience	Cat#0114; Cas#6384-92-5
Tetrodotoxin citrate (TTX)	Biotrend	Cat# ARCD-0640-1; Cas#18660-81-6
Tetrodotoxin citrate (TTX)	HelloBio	Cat#HB1035; Cas#18660-81-6
Triton X-100	Sigma-Aldrich	Cas#9036-19-5
2-methylbutane	Merck KGaA	Cas#78-78-4
DAPI	Sigma-Aldrich	Cas#28718-90-3
Fluoromount-G	SouthernBiotech	Cat#0100-01
Agarose	Sigma-Aldrich	Cas#9012-36-6
Normal donkey serum (NDS)	Merck KGaA	Cat#566460
Experimental models: Organisms/strains		
Mouse line (*B6.129S2-Emx1$^{tm1(cre)Krj}$/J* or *Emx1^{IREScre}*)	The Jackson Laboratory	RRID: IMSR_JAX:005628
Mouse line (*B6;129S6-Gt(ROSA)26Sor$^{tm96(CAG- GCaMP6s)Hze}$/J* or *GCaMP6s^{LSL}*)	The Jackson Laboratory	RRID: IMSR_JAX:024106
Mouse line (C57BL/6J)	The Jackson Laboratory	RRID: IMSR_JAX:000664
Software and algorithms		
LabChart 8	ADInstruments	RRID: SCR_023643
MES 8.3	Femtonics	RRID: N/A
MESc 3.5	Femtonics	RRID: N/A
ZEN 3.1	Carl Zeiss AG	RRID: N/A
pClamp (Clampfit)	Molecular Devices	RRID: SCR_011323
Patchmaster	HEKA Elektronik	RRID: SCR_000034
Mini Analysis Program	Synaptosoft	RRID: SCR_002184
OriginPro	OriginLab	RRID: SCR_014212
IBM SPSS Statistics	IBM	RRID: SCR_016479
MATLAB	Mathworks	RRID: SCR_001622
Fiji	fiji.sc/	RRID: SCR_002285
ComDet package in Fiji	imagej.net/plugins/spots-colocalization-comdet	N/A

(*Continued on next page*)

Continued

REAGENT or RESOURCE	SOURCE	IDENTIFIER
CATHARSiS	github.com/kirmselab/CATHARSiS	https://doi.org/10.5281/zenodo.13767254
NoRMCorre	github.com/flatironinstitute/NoRMCorre	https://doi.org/10.1016/j.jneumeth.2017.07.031
Gini coefficient	de.mathworks.com/matlabcentral/fileexchange/28080-gini-coefficient-and-the-lorentz-curve	N/A

EXPERIMENTAL MODEL AND STUDY PARTICIPANT DETAILS

All animal procedures were performed with approval of the local governments (Thüringer Landesamt für Verbraucherschutz, reference no.: 02–012/16; Regierung von Unterfranken, Arbeitsbereich Tierschutz, reference no.: RUF-55.2.2-2532-2-1567) and complied with European Union norms (Directive 2010/63/EU). Animals were housed in standard open cages with *ad libitum* access to food and water (12/12 h light–dark cycle; temperature: 22 ± 2°C; humidity: 50–60%). *Emx1*^{IREScre} (#005628) and *GCaMP6s*^{LSL} (#024106) mice were originally obtained from The Jackson Laboratory and maintained on a C57BL/6J background. Double heterozygous offspring (*Emx1*^{IREScre}*::GCaMP6s*^{LSL} mice for Figures 1, 4, S1, S2, and S4; C57BL/6J for Figure 2) were used for experiments. Mice of either sex were used. For each experimental dataset, the age of mice is specified in results.

METHOD DETAILS

Murine placental passive-transfer model

For the placental passive-transfer model, previously isolated monoclonal human IgG1 antibodies were used, either the NR1-reactive clone #003–102 derived from a patient with anti-NMDAR encephalitis[49] or the isotype-matched non-reactive control clone #mGO53.[50] Monoclonal #003–102 has been shown to induce NMDAR hypofunction, reducing surface and synaptic receptor levels and diminishing NMDA-evoked currents through receptor antagonism.[5,36] At the network level, #003–102 disrupts excitatory–inhibitory dynamics and increases hypersynchrony and hyperexcitability in rodent models of NMDAR encephalitis,[8,9] and high-resolution imaging demonstrates early alterations in NMDAR membrane organization that precede synaptic receptor loss.[51]

Recombinant antibodies were generated by transient transfection of paired heavy- and light-chain expression vectors into HEK293T cells, followed by purification from culture supernatants using Protein G Sepharose and quantification with an anti-human IgG ELISA (Mabtech, 3850-1AD-6).

Breeders were paired for one day, and the day of separation was designated as E0. Timed-pregnant mice received intraperitoneal injections of either #003-102[49] or #mGO53[50] ABs on E14 and E17 (240 μg each, in phosphate-buffered saline [PBS]).[36] AB amounts were the same as used in our previous study, which yielded maternal serum NR1 AB titers of 1:100 to 1:320 in routine cell-based assays,[36] i.e., within the range of seropositive patients with NMDAR encephalitis.

Serum sampling and ELISA quantification

Trunk blood was collected from the offspring following decapitation at P0 and P5, respectively. Samples were kept on ice for at least 30 min to allow clot formation before being centrifuged (Centrifuge 5430/5430, Eppendorf AG) at 2000 g for 10 min at 4°C. Serum samples were stored at −20°C until further use. Human IgG levels were determined using a commercial anti-human IgG enzyme-linked immunosorbent assay (Mabtech, ref. 380-1AD-6). In brief, 8 μL of murine serum were diluted into 200 μL of PBS containing 0.05% Tween 20 and 0.1% bovine serum albumin. From this initial dilution, three additional 2.5-fold serial dilutions were prepared and IgG concentrations were determined according to the manufacturer's instructions, all as previously described.[49]

Immunohistochemistry and confocal imaging

Animals were decapitated under deep isoflurane anesthesia. The brains were quickly removed in ice-cold PBS and immersion fixed in 4% paraformaldehyde (PFA) for 5 h at 4°C at postnatal 0 (P0). Tissues were cryoprotected by immersing in 10% and subsequently in 30% sucrose/PBS (w/v) overnight at 4°C. Tissue blocks were snap-frozen in 2-methylbutane chilled with dry ice. Coronal sections (40 μm) comprising the hippocampus were prepared on a cryomicrotome (Microm KS34, Thermo Fisher Scientific). Free-floating sections were stored in anti-freeze solution at −20°C until immunostaining. Sections were rinsed in PBS and permeabilized with 0.2% Triton X-100 in PBS for 30 min prior to blocking in a solution containing 3% normal donkey serum and 0.2% Triton X-100 in PBS at room temperature. Sections were incubated at room temperature for 3 h with secondary antibody Alexa Fluor 647 goat anti-human IgG (1:500, Invitrogen, #A-21445; RRID: AB_2535862) in PBS supplemented with 3% normal donkey serum/0.2% Triton X-100. Next, sections were rinsed in PBS and transferred to microscope slides in gelatin. The slides were allowed to dry at room temperature prior to washing in PBS. Nuclei were counterstained with DAPI. Finally, slides were washed in PBS and mounted using

Fluoromount-G. Confocal images of the neonatal hippocampus were acquired on a Zeiss LSM 900 laser-scanning confocal microscope using an LD LCI Plan-Apochromat 40×/1.2 multi-immersion objective.

Preparation of acute brain slices

Animals were decapitated under deep isoflurane anesthesia. The brain was quickly removed and transferred into ice-cold saline containing (in mM): 125 NaCl, 4 KCl, 10 glucose, 1.25 NaH_2PO_4, 25 $NaHCO_3$, 0.5 $CaCl_2$, and 6 or 2.5 $MgCl_2$, gassed with carbogen (5% CO_2, 95% O_2; pH 7.4).[44] Horizontal brain slices (350 μm) were cut on a vibratome and stored for at least 1 h before their use at room temperature (alternatively, for 30 min at ∼32°C and then at room temperature for at least 30 min) in artificial cerebrospinal fluid (ACSF) containing (in mM): 125 NaCl, 4 KCl, 10 glucose, 1.25 NaH_2PO_4, 25 $NaHCO_3$, 2 $CaCl_2$, and 1 $MgCl_2$, gassed with carbogen (pH 7.4). For recordings, slices were transferred into a submerged-type recording chamber on the microscope stage. All experiments were performed at ∼32°C. Of note, we used horizontal hippocampal slices because this orientation preserves the CA3–CA1 and extrahippocampal connectivity required for reliable GDP generation,[44] whereas coronal slices yielded GDPs only inconsistently in our hands. This slicing plane resulted in recordings being centered on the intermediate hippocampus. Thus, *ex vivo* data do not exclusively reflect dorsal CA1, which was the focus of the *in vivo* imaging.

Two-photon Ca^{2+} imaging *ex vivo*

Single-cell Ca^{2+} imaging was performed on *Emx1*+ GCaMP6s-expressing cells in stratum pyramidale of hippocampal CA1 (*Emx1*^{IREScre}*::GCaMP6s*^{LSL} mice). Imaging was performed using an acousto-optic deflection (AOD) two-photon laser-scanning microscope operated by the software MES (Femto3D ATLAS, Femtonics). Fluorescence excitation at 920 nm was provided by a tunable Ti:Sapphire laser (Chameleon Ultra II, Coherent) using a 20×/1.0 NA water immersion objective (XLUMPLFLN 20XW, Olympus). Emission light was detected by photomultiplier tubes (16 bit, H11706P-40, Hamamatsu) above and below the sample. In the upper detection pathway, emission light was separated from excitation light using a primary dichroic mirror (700 nm), short-pass filtered with an IR blocker (700 nm) and further band-pass filtered (520/60 nm). In the lower detection pathway, an oil immersion condenser was used. Excitation light was blocked using an IR blocker (700 nm). The emission light was then passed through a dichroic mirror (565 nm) and band-pass filtered (520/60 nm). Signals from both photomultiplier tubes were summed up by a signal combiner and digitized. Images were acquired from a field of view of 329.2 × 329.2 μm (750 × 750 pixels). Sampling rate was set to approximately 9.3 Hz. Spontaneous activity was recorded for approximately 10 min per field of view and condition. A single field of view was analyzed per slice.

For recording NMDA-evoked somatic CaTs, a $MgCl_2$-free ACSF was used, supplemented with TTX (0.5 μM) and nifedipine (10 μM) to block voltage-gated Na^+ and L-type Ca^{2+} channels, respectively. Following a 60-s baseline period, NMDA (10 μM) was bath-applied for 60 s, and fluorescence was continuously recorded until NMDA washout.

Patch-clamp recordings *ex vivo*

Electrophysiological signals were acquired using a HEKA EPC 10 amplifier, a built-in 16-bit AD/DA board and the software Patchmaster (HEKA Elektronik). Signals were low-pass filtered at 2.9 kHz and sampled at 20 kHz. AMPAR-mediated mEPSCs and $GABA_A$R-mediated mGPSCs were recorded using the whole-cell patch-clamp technique. The intra-pipette solution contained (mM): 145 CsCl, 5 NaCl, 10 HEPES, 2 QX-314, 0.2 EGTA, 1.8 Mg-ATP, 0.3 Na-GTP (pH 7.3 with CsOH). For recording mEPSCs, tetrodotoxin (TTX, 0.5 μM), APV (50 μM) and gabazine (10 μM) were added to the ACSF to block voltage-gated Na^+ channels, NMDA and $GABA_A$Rs, respectively. For recording mGPSCs, TTX (0.5 μM), APV (50 μM) and DNQX (10 μM) were added to the ACSF to block voltage-gated Na^+ channels, NMDARs and AMPARs, respectively. Pipette resistance was 3–5 MΩ when filled with the above solution. Holding potential was set to −70 mV (not corrected for liquid junction potential). Access resistance was monitored by applying hyperpolarizing pulses of 10 mV. Recordings started at 5 min after membrane rupture. Only recordings with an access resistance below 30 MΩ were accepted. Series resistance compensation was not applied.

Surgery, anesthesia and animal monitoring

For analgesia, a subcutaneous injection of 200 mg/kg metamizol (Novacen) was administered 30 min prior to the start of the preparation. Animals were then placed onto a warm platform and anesthetized with isoflurane (3.5% for induction, 1–2% for maintenance) in pure oxygen (flow rate: 1 L/min). The skin overlying the skull was disinfected and locally infiltrated with 2% lidocaine (s.c.) for local analgesia. Scalp and periosteum were removed, and a custom-made plastic chamber with a central borehole (Ø 3.5 mm) was fixed on the skull using cyanoacrylate glue (UHU) (P10–11: 2.5 mm rostral from lambda and 2 mm lateral from midline; P22–24: 2.5 mm rostral from lambda and 2 mm lateral from midline). For the hippocampal window preparation,[44] the plastic chamber was tightly connected to a preparation stage and subsequently perfused with warm ACSF containing (in mM): 125 NaCl, 4 KCl, 25 $NaHCO_3$, 1.25 NaH_2PO_4, 2 $CaCl_2$, 1 $MgCl_2$ and 10 glucose, constantly gassed with carbogen (pH 7.4, 35°C–36°C). A circular hole was drilled into the skull using a tissue punch (outer diameter 2.7 mm). The underlying cortical tissue and parts of corpus callosum were carefully removed by aspiration using a vacuum supply and a blunt 27G or 30G needle. Care was taken not to damage alveus fibers. As soon as the bleeding stopped, ACSF was removed, and the animal was transferred to the microscope stage. The hippocampal window was filled with a droplet of 1.5% agarose (diluted in 0.9% NaCl) and sealed with a glass coverslip. The head-fixed plastic chamber was perfused with ACSF, constantly gassed with carbogen (pH 7.4, at 35°C–36°C). During *in vivo* recordings, body temperature

was continuously monitored and maintained at close to physiological values (36°C–37°C) by means of a heating pad and a temperature sensor placed below the animal. Spontaneous respiration was monitored using a differential pressure amplifier (Spirometer Pod and PowerLab 4/35, ADInstruments). Isoflurane was discontinued after completion of the surgical preparation and gradually substituted with the analgesic-sedative nitrous oxide (up to the fixed final N_2O/O_2 ratio of 3:1, flow rate: 1 L/min). Experiments commenced 60 min after withdrawal of isoflurane. At the end of the experiment, the animal was decapitated under deep isoflurane anesthesia.

Two-photon Ca^{2+} imaging *in vivo*

Single-cell Ca^{2+} imaging was performed on *Emx1*+ GCaMP6s-expressing cells in stratum pyramidale of hippocampal CA1 (*Emx1*^{IREScre}*::GCaMP6s*^{LSL} mice) as described above ('Two-photon Ca^{2+} imaging *ex vivo*'), except for the following differences. Emission light was detected by a single photomultiplier tube (16 bit, H11706P-40, Hamamatsu) above the sample. Sampling rate was set to approximately 38.8 Hz (366 × 366 pixels, 329.2 × 329.2 μm). Spontaneous activity was recorded for at least 60 min per field of view. A single field of view was analyzed per mouse.

QUANTIFICATION AND STATISTICAL ANALYSIS

ELISA quantification

For each serum sample four 2.5-fold dilutions were generated and the IgG concentration was calculated as the mean of the values obtained from dilutions with optical density (OD) readings falling within the linear range of the plate-specific IgG reference curve. IgG concentrations above 90 μg/mL were considered beyond the assay's upper limit of quantification.

Immunohistochemistry

Quantification of human IgG puncta density was performed using the ComDet package in Fiji. Confocal images of the hippocampus contain the Alexa Fluor 647 (red) channel and the DAPI channel. In each confocal image file, based on morphological information from the DAPI channel, regions of interest (ROIs, each 31.2 μm × 31.2 μm, 100 × 100 pixels) representing strata oriens, pyramidale, radiatum and lacunocum-moleculare were drawn along an axis perpendicular to the CA1 pyramidal cell layer. For each CA1 layer, three non-overlapping ROIs were defined (12 ROIs per image file in total). The ROIs from the red channel were then cropped, and puncta were detected separately for each ROI using the ComDet algorithm at an identical detection threshold.

Patch-clamp recordings

mPSCs were visually preselected and semi-automatically detected based on an amplitude and area criterion using Mini Analysis Program 6.0 (Synaptosoft). Quantal amplitude was estimated by the median mPSC amplitude per cell. Decay kinetics was quantified by the mean half-decay time. Passive properties were determined from current responses to de- or hyperpolarizing (10 mV) steps in voltage-clamp mode. Series (R_s) and membrane (R_m) resistance were estimated from the amplitude of the capacitive transient and the steady-state current, respectively. The decay of the capacitive transient was fitted with a two-term exponential function, and membrane capacitance (C_m) was obtained as the ratio of the weighted time constant and R_s. The membrane time constant (τ_m) was determined as the product of R_m and C_m.

Two-photon Ca^{2+} imaging

Preprocessing and CaT detection

Image stacks were registered using NoRMCorre.[95] Under nitrous oxide, pups spend most of the of time in a quiet or minimally active (sleep) state, consistent with previous observations.[44,46] However, locomotion was frequently accompanied by z-drift in the recorded field of view, making extraction of CaTs impossible. Time periods with residual z-drift were visually identified and considered as missing values in all subsequent analyses. Therefore, our analysis was effectively restricted to motion-free epochs in which network activity could be assessed reliably, but we acknowledge that behavioral state could still represent a potential confound.

Regions of interest (ROIs) corresponding to the somata of GCaMP6s-expressing CA1 PCs were manually selected (Fiji). Onsets of somatic CaTs were detected using CATHARSiS ('Calcium transient detection harnessing spatial similarity'), which enables the reliable reconstruction of somatic CaTs in densely labeled tissue with both high detection and temporal accuracies.[46] For each cell, reconstructed CaT onsets were translated into a binary activity vector (1 – event, 0 – no event) and used for subsequent analyses.

Network bursts (GDPs) ex vivo

In acute slice recordings, GDPs were defined as a significant co-activation of CA1 PCs as follows: (1) To account for some temporal jitter in CaT detection, all values in the binary activity vectors that fell within $\pm\Delta t$ frames of any detected CaT were set to 1. Here, Δt was set to 3 frames (322 ms). We then computed the mean across the resulting activity vectors of all individual CA1 PCs to obtain the empirical fraction of active cells per frame $\Phi(t)$. (2) We randomly shuffled CaT onsets of all cells (uniform distribution; 1,000 iterations), computed the surrogate $\Phi(t)$ and defined the 99.99th percentile of all surrogate $\Phi(t)$ values as the threshold for GDP detection. The GDP threshold was determined separately for each FOV to account for differences in mean CaT frequencies. (3) Any frame with an empirical $\Phi(t)$ exceeding the threshold was considered as belonging to a GDP. In the resulting binary GDP vectors, 0–1 transitions

were defined as GDP onsets and 1-0 transitions as GDP offsets. GDP size was defined as the fraction of cells which were active in at least one frame of a given GDP, corrected for the chance level of co-activation by subtracting the GDP threshold.

NMDA-induced somatic CaTs

To quantify NMDA-induced CaTs, raw fluorescence traces were first smoothed using a Savitzky-Golay filter (window length: 100 frames). Baseline fluorescence (F_0) was determined by linear fitting of the initial and final 1000 frames of each trace, excluding the lowest and highest 25% of data points to minimize noise. Relative fluorescence changes ($\Delta F/F_0$) were computed, and NMDA-evoked responses ($\Delta F/F_0$) were quantified by extracting peak amplitude and area under the curve.

Firing statistics of pyramidal cells

For each PC, we quantified its firing irregularity by applying CV and CV2 measures to its detected CaT onsets.[46,59] CV2 is a local and relatively rate-independent measure of spike-time irregularity: $CV2 = \frac{2}{K-1}\sum_{k=1}^{K-1}\frac{|ICI_{k+1}-ICI_k|}{ICI_{k+1}+ICI_k}$, where ICI_k and ICI_{k+1} are the k^{th} and $(k+1)^{th}$ ICIs of the cell, and K is the total number of its ICIs. Conversely, CV quantifies the global irregularity of spike-times and is computed using the coefficient of variation as $CV = \sigma_{ICI}/\mu_{ICI}$, where σ_{ICI} and μ_{ICI} are the standard deviation and mean of ICIs. We further quantified each cell's instantaneous CaT frequency (f_{CaT}) as the median of its instantaneous frequencies $f_k=(1/ICI_k)$, where $k = 1, 2, \ldots, K$.

Discontinuous and continuous network activity

To define periods of *in vivo* discontinuous or continuous network activity, we expanded the binary activity vectors of all cells using a ±12-frame (±0.32 s) window. We then computed the mean of these expanded vectors across cells to generate a population activity measure, Φ(t). Next, Φ(t) was partitioned into non-overlapping 388-frame (∼10 s) bins. Bins with >10% missing values (due to z-drift) were excluded from analysis. For each included bin, baseline activity (Φ_0) was estimated as the 20^{th} percentile of its Φ(t) values. Bins were classified as continuous if Φ_0 exceeded 2%; otherwise, they were classified as discontinuous. Time in continuous activity was quantified as the percentage of continuous bins among included bins. To decouple the operational classification of bins from CaT rate differences, we repeated this analysis for randomly shuffled data (uniform distribution; 1,000 iterations) and used the mean time in continuous activity as a statistical covariate. To test for the robustness of our findings, we used an alternative classification, where Φ_0 was estimated as the mode of Φ(t), with a threshold of 3% for continuous activity.

Pairwise coupling

We quantified pairwise neuronal coupling using the spike time tiling coefficient (STTC).[60] The synchronicity window Δt was varied from ∼0.3 s to ∼5.2 s for both *ex vivo* and *in vivo* datasets.

Network coupling

To quantify the degree of functional interaction between any *i*th cell and its local network, we determined its network coupling, Net-$C_{emp,i}$, as the Pearson correlation coefficient between the smoothed version of its CaT train, S_i, and of the summed activity of the rest of population, $S_{tot\setminus i}$; for related measures, see.[46,96,97] For smoothing, we used a Gaussian kernel, whose standard deviation (SD) determines the timescale of coupling to be assessed. Raw Net-$C_{emp,i}$ values can be confounded by the cell's mean CaT rate or, more generally, through by-chance coordination of its activation times with the network-level activity. Therefore, to correct for such potential biases, we used two types of surrogate data (for a graphical representation, see Figure 4M; Figures S4I and S4K). (i) Circular shuffling, which shifts each binary CaT train by a random number of frames (uniformly distributed), wrapping excess beyond the original train-length to the beginning. This method preserves both the timing and average rate of cell's CaTs. (ii) Random shuffling, which randomly re-distributes the timing of cell's CaTs, thus preserving only its average CaT rate but not the ICIs. Both methods destroy the cell's CaT timing relative to the rest of population. This enables the computation of its chance-level coupling, Net-$C_{shuff,i}$, as the correlation coefficient between the smoothed, shuffled CaT train and the empirical $S_{tot\setminus i}$. This process is repeated multiple times, followed by computing the median bias over the repetitions, Net-$C_{shuff,i}$. Taken together, the bias-corrected network coupling of the cell of interest (COI) is obtained by Net-C_{COI} = Net-$C_{emp,i}$ - Net-$C_{shuff,i}$. Finally, we used event-exchange shuffling method to assess the importance of population-level coordinated activities in governing the network coupling of each individual cell. This method randomly exchanges the timing of CaTs across all cells, thereby destroying the cell's CaT timing relative to the rest of population. However, it preserves not only the cell's mean CaT rate but also the summed population activity per time-point. Upon multiple shuffling repetitions, the Net-C_{COI} is computed similarly to above. In this case, a relatively small (near-zero or negative) Net-C_{COI} can imply a dominancy of cell's activity by that of the local network. For all shuffling methods, we used 500 repetitions. The computations were performed separately for each, ranging from ∼0.3 to ∼5.2 s.

Neural network modeling

Overview

To investigate the mechanistic links between NR1 AB-induced alterations at cellular and circuit levels in neonatal CA1, we resorted to the computational modeling and stability analysis methods. We employed a data-driven recurrent neural network (RNN) model of population activities during the first postnatal month.[48] It is an extended Wilson-Cowan-type model,[98] and thus benefits from being biophysically interpretable and mathematically accessible. We consider here the RNN which has been successfully adapted to explain the key dynamics and mechanisms of GDPs in neonatal CA1 with excitatory GABA signaling during the first postnatal week.[58] In the following, after providing the mathematical description of the model, we describe the mathematical components used for its stability analysis and simulations. For more details about the model and the approach see.[48]

Model description

The RNN is a mean-field network model of average firing activity rates of two spatially localized, homogeneous glutamatergic (PC) and GABAergic interneuron (GIN) cell populations that are recurrently connected. The model incorporates two short-term synaptic plasticity (STP) mechanisms, namely short-term synaptic depression (STD) and facilitation (STF), which render the synaptic efficacies dynamic over time. Hence, we call the network hereafter STP-RNN. The 10D system of equations governing the mean-field dynamics of the STP-RNN are (dots denote the time derivatives, and hereafter, PC and GIN are abbreviated as P and G for readability) (Equation 1):

$$\begin{aligned}
\tau_P \dot{A}_P(t) &= -A_P(t) + f_P\left(J_{PP}u_{PP}(t)x_{PP}(t)A_P(t) - J_{PG}u_{PG}(t)x_{PG}(t)A_G(t) + e_P(t)\right) = -A_P(t) + f_P(h_P)\\
\tau_G \dot{A}_G(t) &= -A_G(t) + f_G\left(J_{GP}u_{GP}(t)x_{GP}(t)A_P(t) - J_{GG}u_{GG}(t)x_{GG}(t)A_G(t) + e_G(t)\right) = -A_G(t) + f_G(h_G)\\
\dot{x}_{ij} &= \tau_{r_{ij}}^{-1}\left(1 - x_{ij}(t)\right) - u_{ij}(t)x_{ij}(t)A_j(t)\\
\dot{u}_{ij} &= \tau_{f_{ij}}^{-1}\left(U_{ij} - u_{ij}(t)\right) + U_{ij}\left(1 - u_{ij}(t)\right)A_j(t)
\end{aligned} \qquad \text{(Equation 1)}$$

where i and $j \in \{P,G\}$, and j is the index of the presynaptic population, A_P and A_G are the instantaneous average activity rates (in Hz) of PC and GIN populations which can be properly scaled to represent locally the average recorded activities of these populations, x_{ij} and u_{ij} are the average dynamic variables of STD and STF mechanisms, τ_P and τ_G are approximations to the time constants of cell population activities, $\tau_{r_{ij}}$ is the synaptic recovery time constant of depression, $\tau_{f_{ij}}$ is the synaptic facilitation time constant, U_{ij} is analogous to the synaptic release probability, J_{ij} is the average maximum absolute synaptic efficacy of recurrent ($i = j$) or feedback ($i \neq j$) connections, and e_P and e_G are the average external inputs received by the PC and GIN populations from other brain regions or stimulation. Here, we model each input as an excitatory pulse (positive amplitude, $e_P = e_G = 3$ Hz) with zero baseline and a duration of 20 ms,[46] thereby emulating e.g., the spontaneous SPW-driven inputs to the PC and GIN populations. The transformation from the total summed input to each population, h_i, to an activity output (in Hz) is governed by the response function, f_i, defined as (Equation 2):

$$f_i(h_i) = \begin{cases} 0 & \text{for } h_i \leq \theta_i \\ g_i(h_i - \theta_i) & \text{for } \theta_i < h_i \end{cases} \qquad \text{(Equation 2)}$$

where θ_i is the population activity threshold, and g_i is the linear input-output gain above θ_i. In this work, we parameterize the STP-RNN as a network model representing mainly a stage during the first postnatal week. To do this, we followed previous work[58] by setting $\tau_P = 0.045$s, $\tau_G = 0.0225$s, $J_{PP} = J_{GP} = J_P = 2$, $J_{GG} = J_{PG} = J_G = -1.7$, $\tau_{r_{PP}} = \tau_{r_{GP}} = \tau_{r_P} = 5.5$ s, $\tau_{r_{GG}} = \tau_{r_{PG}} = \tau_{r_G} = 5$ s, $\tau_{f_{PP}} = \tau_{f_{GP}} = \tau_{f_P} = 0.8$ s, $\tau_{f_{GG}} = \tau_{f_{PG}} = \tau_{f_G} = 0.8$ s, $U_{PP} = U_{GP} = U_P = 0.9$, $U_{GG} = U_{PG} = U_G = 0.9$, $\theta_P = 0.3$, $\theta_G = -0.1$, $g_P = g_G = 1$, and $e_P = e_G = 0$ Hz (for spontaneous baseline activity). According to these parameter values, both glutamatergic and GABAergic connections will act as depressing, and GABAergic transmission will be excitatory (note the negative value of J_G). We consider the STP-RNN with these parameter values as the "default model". To emulate the NR1 AB-induced alterations observed in our electrophysiological data (see results), we considered the following re-parameterizations of the default model: I) $J_{PG} \rightarrow \kappa_J \times J_{PG}$, II) $U_{PG} \rightarrow \kappa_U \times U_{PG}$, and III) $\tau_P \rightarrow \kappa_\tau \times \tau_P$, where κ_J, κ_U and κ_τ are some constant scaling factors. Based on these data, we set $\kappa_J = 0.5$ and $\kappa_\tau = 1.5$ for model 2, and $\kappa_U = 0.5$ and $\kappa_\tau = 1.5$ for model 3 (see Figure 3). For the robustness analysis, these scaling factors were varied in plausible ranges (see the color-coded matrices in Figure 3). In addition, to assess the robustness of the model findings given the relatively low recurrent excitatory connectivity of CA1, we performed a sensitivity analysis by varying J_{PP} between 20% and 100% of the default value ($J_{PP} = 2$) across all three models, while maintaining all other parameters constant. In all models with reduced J_{PP}, simGDPs were still evoked by brief inputs delivered to the PC and GIN populations (Figures S3A–S3D). This reflects an experimental constraint, as CA1 is known to be capable of generating GDPs even after mechanical disconnection from CA3.[58,99,100]

Frozen STP-RNN

A Frozen STP-RNN is obtained by freezing the synaptic efficacies of an STP-RNN; i.e., by fixing the STP variables x_{ij} and u_{ij} at the values of interest. This will convert the STP-RNN (10D; see Equation 1) effectively to a 2D network with constant synaptic weights. As shown in previous studies,[46,48,58] the Frozen STP-RNN can provide a reliable approximation to the stability behavior of an STP-RNN at the activity-state chosen for freezing (see below). The equations governing the dynamics of a Frozen STP-RNN are (Equation 3):

$$\begin{aligned}
\tau_P \dot{A}_P(t) &= -A_P(t) + f_P\left(J_{PP}^{frz}A_P(t) - J_{PG}^{FP}A_G(t) + e_P(t)\right)\\
\tau_G \dot{A}_G(t) &= -A_G(t) + f_G\left(J_{GP}^{frz}A_P(t) - J_{GG}^{frz}A_G(t) + e_G(t)\right)
\end{aligned} \qquad \text{(Equation 3)}$$

where $J_{ij}^{frz} = J_{ij}u_{ij}^{frz}x_{ij}^{frz}$, and u_{ij}^{frz} and x_{ij}^{frz} are the values of u_{ij} and x_{ij} (see Equation 1), here, at the rest state; i.e., prior to the external inputs arrival, where $e_P = e_G = 0$ and all network dynamic variables are already at their steady state values (see results).

Phase plane

To visualize the stability behavior of the network model, we used the phase plane analysis of the Frozen STP-RNN, based on the activity rates: A_G-A_P-plane (2D). The A_G-A_P-plane sketch includes the curves of the A_P-nullcline and A_G-nullcline representing sets of points for which $\dot{A}_P(t) = 0$ and $\dot{A}_G(t) = 0$ in the corresponding Frozen STP-RNN (thus, 2D; see Equation 3), respectively. Any intersection of these nullclines is called a fixed point (FP; or steady state), with the stability needed to be determined (see below). These FPs may include not only the rest state of the full network but also some other FPs which may not exist in the STP-RNN itself.[46,48,58] In

addition to the visualization of the FPs in the A_G-A_P-plane, we also computed the FPs by numerically solving Equation 3 after setting the right-hand side of the equations to zero; for more details, see.[48]

Stability of FPs

To determine the stability of any FP in the STP-RNN (resp. in the Frozen STP-RNN) we applied the linear stability analysis to its 10D (resp. 2D) system of equations in Equation 1 (resp. Equation 3): We investigated whether all eigenvalues of the corresponding Jacobian matrix have strictly negative real parts (if so, the FP is stable), or whether at least one eigenvalue with a positive real part exists (if so, the FP is unstable).

Simulations

All simulation results in this study have been implemented as Mathematica and MATLAB (MathWorks) code. For network simulations, we set the integration time-step size to 0.0002 s.

Statistical analysis

Statistical analyses were performed using OriginPro and IBM SPSS Statistics. Detailed statistical information, including biological replicates, is provided in Tables S1, S2, and S3. *p* values (two-tailed tests) below 0.05 were considered statistically significant. For two-group comparisons, data normality was assessed using the Shapiro-Wilk test. Parametric tests were applied to normally distributed data; otherwise, non-parametric alternatives were used. For comparisons involving two independent variables, two-way analysis of variance (ANOVA) was performed. When ANOVA assumptions were violated, data were fitted with generalized linear models (GLMs), with the dependent variable modeled as normal (with identity link) or gamma (with log link) distribution, based on *a priori* considerations and goodness-of-fit evaluation. In some cases, covariates were included as indicated in the results section (see Tables S1, S2, and S3). Overall model significance was assessed using the likelihood ratio chi-square test. Fixed effects were only evaluated if the overall model was significant. If the overall model and the interaction term were significant, simple contrasts were computed to assess the effect of one factor at specific levels of the other. To prevent overfitting, non-significant interaction terms were removed using hierarchical model selection. A generalized linear mixed model (GLMM) was used to analyze human IgG puncta densities across hippocampal layers, with 'treatment', 'layer' and their interaction modeled as fixed effects, and 'mouse ID' included as a random effect to account for within-subject variability. Model evaluation followed the same principles outlined above for GLMs. To analyze Net-C and STTC across timescales, we first computed a GLMM, with 'treatment', 'age', 'SD' (or 'Δt') and all possible interactions as fixed effects, and 'mouse ID' included as a random effect. We again applied hierarchical model selection to remove non-significant interaction terms. If both the overall model and an interaction term were significant, we followed up by computing separate GLMs for each level of 'SD' (or 'Δt').